Saturation of a turbulent mixing layer over a cavity: response to harmonic forcing around mean flows

Edouard Boujo, Michaël Bauerheim, Nicolas Noiray

To cite this version:

Edouard Boujo, Michaël Bauerheim, Nicolas Noiray. Saturation of a turbulent mixing layer over a cavity: response to harmonic forcing around mean flows. Journal of Fluid Mechanics, 2018, 853, pp.1-35. ⟨10.1017/jfm.2018.568⟩. ⟨hal-02114962⟩

HAL Id: hal-02114962

https://hal.science/hal-02114962v1

Submitted on 30 Apr 2019

Official URL: https://doi.org/10.1017/jfm.2018.568

To cite this version :

Boujo, Edouard and Bauerheim, Michaël and Noiray, Nicolas Saturation of a turbulent mixing layer over a cavity: response to harmonic forcing around mean flows. (2018) Journal of Fluid Mechanics, 853. 1-35. ISSN 0022-1120

Saturation of a turbulent mixing layer over a cavity: response to harmonic forcing around mean flows

E. Boujo, M. Bauerheim and N. Noiray
CAPS Lab., Mechanical and Process Engineering Dept., ETHZ, CH-8092 Zürich, Switzerland

November 2, 2017

Turbulent mixing layers over cavities can couple with acoustic waves and lead to undesired oscillations. To understand the nonlinear aspects of this phenomenon, a turbulent mixing layer over a deep cavity is considered and its response to harmonic forcing is analysed with large-eddy simulations (LES) and linearised Navier–Stokes equations (LNSE). The Reynolds number is Re=150 000. As a model of incoming acoustic perturbations, spatially uniform time-harmonic velocity forcing is applied at the cavity end, with amplitudes spanning the wide range 0.045–8.9% of the main channel bulk velocity. Compressible LES provide reference nonlinear responses of the shear layer, and the associated mean flows. Linear responses are calculated with the incompressible LNSE around the LES mean flows; they predict well the amplification (both measured with kinetic energy and with a proxy for vortex sound production in the mixing layer) and capture the nonlinear saturation observed as the forcing amplitude increases and the mixing layer thickens. Perhaps surprisingly, LNSE calculations based on a monochromatic (single frequency) assumption yield a good agreement even though higher harmonics and their nonlinear interaction (Reynolds stresses) are not negligible. However, it is found that the leading Reynolds stresses do not force the mixing layer efficiently, as shown by a comparison with the optimal volume forcing obtained from a resolvent analysis. Therefore they cannot fully benefit from the potential for amplification available in the flow. Finally, the sensitivity of the optimal harmonic forcing at the cavity end is computed with an adjoint method. The sensitivities to mean flow modification and to a localised feedback (structural sensitivity) both identify the upstream cavity corner as the region where a small-amplitude modification has the strongest effect. This can guide in a systematic way the design of strategies aiming at controlling the amplification and saturation mechanisms.

Key words: aeroacoustics, instability, turbulent flows

---

1 Introduction

Flow over a cavity leads to a variety of interesting phenomena, including radiated noise in the form of broadband and discrete components. Related applications are numerous in aeronautics (wheel wells), ground transportation (pantograph cavities, door gaps, open windows), turbomachinery (bleed slots for secondary air supply in compressors) and other energy-related systems (T-junctions and side branches in pipe networks for air, water, steam or gas). Therefore, it comes as no surprise that, for more than 60 years, many studies have investigated cavity flows. In general, sustained vortical oscillations in the shear layer and acoustic oscillations result from a process involving hydrodynamics and acoustics, although details depend on the specific configuration. (See for instance reviews by [Rockwell and Naudascher, 1978, Rockwell and Naudascher, 1979, Rockwell, 1983, Rowley and Williams, 2006, Tonon et al., 2011, Morris, 2011].) In shallow cavities, vortical disturbances in the shear layer impinge on the downstream cavity corner, and cavity tones may be generated by a feedback mechanism (hydrodynamic/acoustic feedback in incompressible/compressible flows at small/large Mach number). In deep cavities, resonant pipe tones may be generated if a cavity acoustic mode (standing wave) is excited by the shear layer (turbulence-induced broadband excitation and/or instability-induced narrowband excitation).

Many linear models have been developed for predicting oscillation frequencies ([Rossiter, 1964, Tam and Block, 1978, Kooijman et al., 2004, Alvarez et al., 2004]). However, accounting for nonlinear saturation and predicting oscillation amplitude remains a challenge. Full Navier–Stokes simulations are computationally expensive, especially in the turbulent regime, and simpler methods are still few. [Rowley and Williams, 2006] mention a model by [Cain et al., 1996] which "*assumes oscillations at the Rossiter frequencies, and assumed nonlinearities enter through saturation of the shear layer: as the amplitude of oscillation grows, Reynolds stresses increase, and the shear layer spreads, decreasing the amplification rate of disturbances. The total amplification of a disturbance is computed around the loop, and an iterative procedure is used to converge to the final oscillation amplitude*". Because this procedure assumes specific nonlinearities, it may be too simplified to give accurate predictions in a wide range of conditions; however, its description of the saturation mechanism is particularly interesting because it probably captures the key ingredients at play. It also points to a recent study by [Mantič-Lugo and Gallaire, 2016] who used a related description for predicting the hydrodynamic response to harmonic forcing in the laminar flow over a backward-facing step. Their model is a system of two equations: the response to harmonic forcing at frequency ω_1 is given by a linear equation (Navier–Stokes operator linearised around the mean flow), while nonlinear interaction of the response with itself modifies the mean flow. As nonlinear saturation effects increase, the mean flow and the linear response progressively converge (both in the iterative algorithm and in the physical flow) to a steady regime. In this semi-linear self-consistent model, the only assumption is that higher harmonics can be neglected altogether, i.e. they have no effect on the linear response at ω_1, nor on the mean flow correction.

In this paper we consider the flow over a deep cavity at large Reynolds number Re and small Mach number M. The flow can be seen as a system of two coupled elements: the incompressible shear layer (hydrodynamic element), and the compressible volume of fluid inside the cavity (acoustic element). In order to make a first step toward the simple prediction of oscillation amplitudes in aeroacoustic systems, we consider separately the shear layer and the deep cavity. In this study, we treat the cavity as an external element, and we focus specifically on the hydrodynamic response of the shear layer to a prescribed harmonic forcing. This forcing is chosen as a plane wave coming from the cavity end, mimicking the dominant acoustic resonance mode (quarter-wave mode) at frequency ω_1. Motivated by the description mentioned earlier in terms of mean flow and harmonic fluctuations, we consider the linear response around the mean flow. In practice, the response to the prescribed forcing is obtained with the Linearised Navier-Stokes Equations (LNSE) incorporating a turbulence model, while the effect of higher harmonics on the response at ω_1 is neglected. We note that the wavelength of the observed cavity resonance mode is much larger than the shear layer width, such that one can make the compactness assumption, neglect compressibility effects and use incompressible LNSE. For simplicity, the mean flow is taken from nonlinear Navier-Stokes simulations carried out independently with Large-Eddy Simulations (LES) with harmonic forcing at various amplitudes, thus automatically taking into account the effect of higher harmonics on the mean flow.

Our study addresses several questions: is it possible to predict accurately the response of the shear layer at different forcing amplitudes using LNSE around the mean flow? Can the saturation mechanism be captured? Can one neglect the effect of higher harmonics on the linear response? None of these questions has obvious a priori answers. In the laminar regime, linear stability analysis around mean flows has been shown to produce relevant results in some cases while failing in other cases. For instance, the frequency of limit-cycle oscillations in the flow past a circular cylinder is well predicted by the dominant linear eigenvalue calculated around the mean flow ([Barkley, 2006]). This led [Mantič-Lugo et al., 2014] to build a self-consistent model for stability analysis in the same vein as that for harmonic response. [Turton et al., 2015] observes that linear stability analysis around the mean flow in a laminar thermosolutal convection system reproduces well the nonlinear characteristics of travelling waves; it fails, however, to produce meaningful results for standing waves. It was proposed that the reason might lie in the second harmonic being negligible for travelling waves, and non-negligible for standing waves. This is to be related to the earlier weakly nonlinear analysis of [Sipp and Lebedev, 2007], who formulated conditions on the second harmonic for the validity of stability analysis around mean flows, and presented a counterexample in a square open cavity. Recently, [Meliga, 2017] extended the self-consistent model, incorporating the second harmonic. In the turbulent regime, linear stability analysis and linear harmonic response calculations around mean flows are common, both in parallel and global settings ([del Álamo and Jiménez, 2006, Piot et al., 2006, Pujals et al., 2009, Hwang and Cossu, 2010, Marquillie et al., 2011, Meliga et al., 2012, Iungo et al., 2013, Gikadi et al., 2014, Mettot et al., 2014, Oberleithner et al., 2015, Beneddine et al., 2016, Edstrand et al., 2016, Tammisola and Juniper, 2016]). It is not clear, however, if the structure and the amplitude of the response to harmonic forcing are meaningful in general, and if the saturation process can be captured accurately. This is what we assess for the deep cavity of this study.

The paper is organised as follows. The configuration and the mean flow obtained from LES with different forcing amplitudes are presented in § 2. Section 3 is devoted to the mean-flow linear response calculated with the LNSE: the problem formulation and numerical method are detailed in §§ 3.1 and 3.2, respectively. Results and comparison with LES results are given in §§ 3.3-3.4. Next, the effect of higher harmonics is investigated in § 4, in particular via consideration of optimal forcings (resolvent analysis). Finally, § 5 presents results from a sensitivity analysis that identifies regions where a flow modification or a localised feedback have the largest effect on the optimal harmonic response, which provides useful information for control design. Conclusions are drawn in § 6.

2 Geometry and mean flow

We consider a straight rectangular channel of height $D = 62$ mm, featuring on one side a deep cavity of width $W = 30$ mm and depth $H = 90$ mm (aspect ratio $W/H = 0.33$). Both channel and cavity are of spanwise extension $L = 10$ mm. A two-dimensional (2D) cross-section I is shown in figure 1. The x, y and z direction are denoted streamwise, vertical and spanwise, respectively. With an inlet bulk velocity $U_\infty = 56$ m/s and a speed of sound $c_0 = 340$ m/s, the air flow in this channel corresponds to a relatively small Mach number $M = U_\infty/c_0 = 0.16$ and a large Reynolds number $Re = U_\infty W/\nu = 1.5 \times 10^5$.

The effect of an acoustic forcing imposed at the cavity end is investigated by means of three-

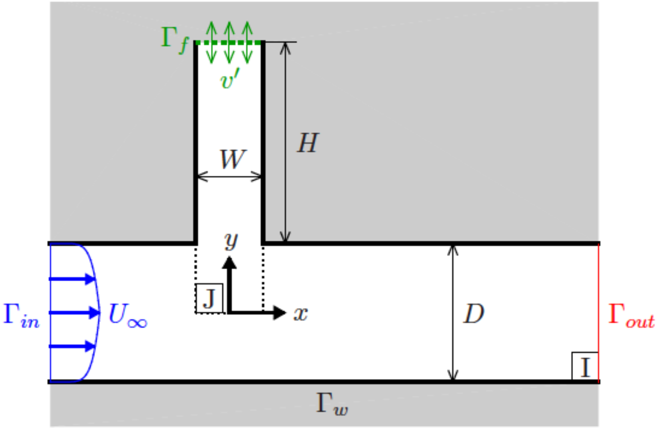

Figure 1: Geometry and flow configuration (see main text for dimensions). LNSE calculations are performed in the 2D domain I, around mean flows from LES performed in a 3D domain (same 2D cross-section I, spanwise extension L). The subdomain J is used in measures (20) and (21) of the response.

dimensional (3D) compressible large-eddy simulations (LES). At the inlet Γ_{in} the incoming flow has a turbulent power-law profile of exponent 0.7. Both inlet Γ_{in} and outlet Γ_{out} are acoustically non-reflecting. A no-slip boundary condition is set on the walls Γ_w. At the cavity end Γ_f, a vertical and spatially uniform, time-harmonic forcing $(0, v'\cos(\omega_1 t), 0)$ is prescribed via a propagative acoustic wave with the NSCBC conditions ([Poinsot et al., 1992]). In this study, the forcing frequency is set to $\omega_1/2\pi = 750$ Hz, close to the frequency of a marginally stable eigenmode and of the largest harmonic response in the unforced flow (see § 3.3). More details about the numerical method are given in [Bauerheim et al., 2017]. The forcing amplitude v' is varied over more than two orders of magnitude, between 0.025 and 5.0 m/s (relative velocity v'/U_∞ between 0.045% and 8.9%).

The LES mean flow obtained for different forcing amplitudes is shown figure 2. The streamwise velocity $\overline{U}$ quickly decreases from U_∞ to 0 in the shear layer. A recirculation region is present inside the cavity, and becomes stronger with the forcing amplitude (maximum negative velocity between -3 and -9 m/s.) As shown in the insets, the shear layer thickens and becomes weaker with x, and the mean spanwise vorticity $\overline{\Omega}_z = \partial_x \overline{V} - \partial_y \overline{U}$ clearly diffuses. Larger forcing amplitudes yield a thicker and weaker shear layer.

3 Linear response of the mean flow to harmonic forcing

3.1 Problem formulation

We start from the Navier–Stokes equations

$$\partial_t \mathbf{U} + \mathbf{N}(\mathbf{U}) = \mathbf{F}, \tag{1}$$

governing the dynamics of velocity $\mathbf{U}(\mathbf{x}, t)$ and pressure $P(\mathbf{x}, t)$, where

$$\mathbf{N}(\mathbf{U}) = (\mathbf{U} \cdot \boldsymbol{\nabla})\mathbf{U} + \frac{1}{\rho}\boldsymbol{\nabla} P - \nu \boldsymbol{\nabla}^2 \mathbf{U}$$

is the nonlinear incompressible Navier–Stokes operator and ρ the fluid density. In this study we restrict our attention to incompressible flows since the Mach number is small, but the

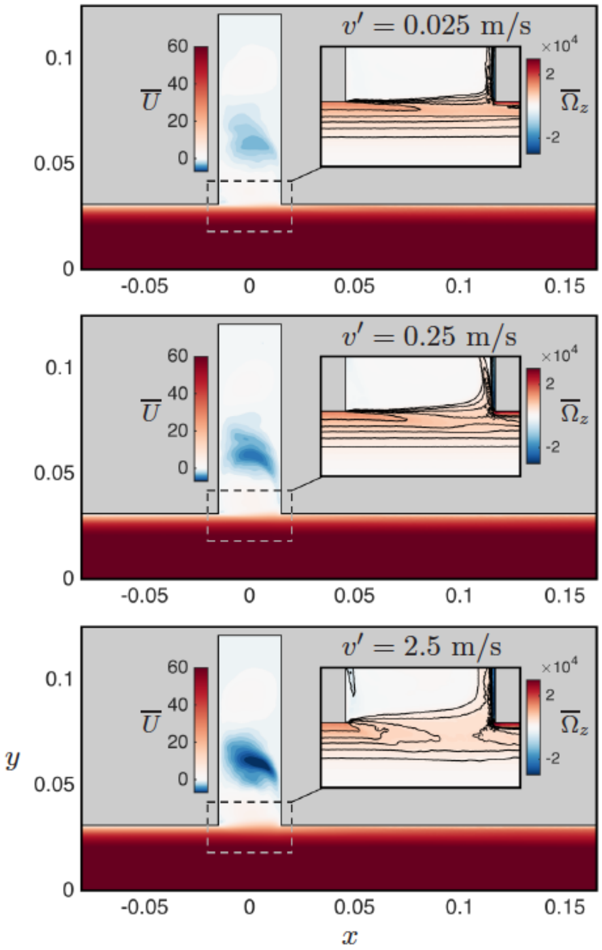

Figure 2: Mean streamwise velocity $\overline{U}$ from LES, at forcing amplitudes $v' = 0.025$, 0.25 and 2.5 m/s. Inset: close-up view of the mean spanwise vorticity $\overline{\Omega}_z = \partial_x \overline{V} - \partial_y \overline{U}$ in the shear layer. Main flow from left to right.

spirit of the derivation is similar for compressible flows. Hereafter, we therefore omit the continuity equation $\boldsymbol{\nabla} \cdot \mathbf{U} = 0$. The term $\mathbf{F}(\mathbf{x}, t)$ denotes a space and time-dependent forcing applied either at a boundary or inside the domain. Following [Reynolds and Hussain, 1972], the flow is decomposed into its time-averaged component $\overline{\mathbf{U}}(\mathbf{x})$, coherent fluctuations $\widetilde{\mathbf{u}}(\mathbf{x}, t)$ and turbulent fluctuations $\mathbf{u}'(\mathbf{x}, t)$:

$$\mathbf{U} = \overline{\mathbf{U}} + \widetilde{\mathbf{u}} + \mathbf{u}'. \tag{2}$$

By construction, time averaging $\bar{\cdot}$ yields the steady mean flow $\overline{\mathbf{U}}$ and removes all fluctuations ($\overline{\widetilde{\mathbf{u}} + \mathbf{u}'} = \mathbf{0}$), while phase averaging $\langle \cdot \rangle$ removes incoherent fluctuations ($\langle \mathbf{U} \rangle = \overline{\mathbf{U}} + \widetilde{\mathbf{u}}$, $\langle \mathbf{u}' \rangle = \mathbf{0}$). (Similar notations are used for other quantities, e.g. pressure, forcing and spanwise vorticity.) Substituting this decomposition into (1) yields coupled equations for the mean flow and coherent fluctuations:

$$\mathbf{N}(\overline{\mathbf{U}}) = -\boldsymbol{\nabla} \cdot \left(\overline{\widetilde{\mathbf{u}}\widetilde{\mathbf{u}}} + \overline{\mathbf{u}'\mathbf{u}'} \right) + \overline{\mathbf{F}}, \tag{3}$$

$$\partial_t \widetilde{\mathbf{u}} + \mathbf{L}(\overline{\mathbf{U}})\widetilde{\mathbf{u}} = -\boldsymbol{\nabla} \cdot \left(\widetilde{\widetilde{\mathbf{u}}\widetilde{\mathbf{u}}} + \widetilde{\mathbf{u}'\mathbf{u}'} \right) + \widetilde{\mathbf{f}}, \tag{4}$$

where $\mathbf{L}(\overline{\mathbf{U}})$ is the Navier–Stokes operator linearised around the mean flow:

$$\mathbf{L}(\overline{\mathbf{U}})\widetilde{\mathbf{u}} = (\overline{\mathbf{U}} \cdot \boldsymbol{\nabla})\widetilde{\mathbf{u}} + (\widetilde{\mathbf{u}} \cdot \boldsymbol{\nabla})\overline{\mathbf{U}} + \frac{1}{\rho}\boldsymbol{\nabla}\widetilde{p} - \nu \boldsymbol{\nabla}^2 \widetilde{\mathbf{u}}. \tag{5}$$

Equation (3) shows that, due to the forcing from the coherent and turbulent Reynolds stresses $\overline{\widetilde{\mathbf{u}}\widetilde{\mathbf{u}}} + \overline{\mathbf{u}'\mathbf{u}'}$, the mean flow $\overline{\mathbf{U}}$ differs from the steady base flow $\mathbf{U}_b$ which is a solution of the stationary Navier–Stokes equations $\mathbf{N}(\mathbf{U}_b) = \overline{\mathbf{F}}$.

Focusing on a coherent time-harmonic forcing at frequency ω_1,

$$\overline{\mathbf{F}} = \mathbf{0}, \quad \widetilde{\mathbf{f}}(\mathbf{x}, t) = \widetilde{\mathbf{f}}_1(\mathbf{x}) e^{i\omega_1 t} + c.c., \quad \mathbf{f}' = \mathbf{0}, \tag{6}$$

where *c.c.* stands for complex conjugate, the coherent response is assumed to fluctuate at the forcing frequency and higher harmonics:

$$\widetilde{\mathbf{u}}(\mathbf{x}, t) = \sum_{n \neq 0} \widetilde{\mathbf{u}}_n(\mathbf{x}) e^{in\omega_1 t} = \sum_{n > 0} \widetilde{\mathbf{u}}_n(\mathbf{x}) e^{in\omega_1 t} + c.c. \quad (\widetilde{\mathbf{u}}_{-n} = \widetilde{\mathbf{u}}_n^*). \tag{7}$$

Introducing this Fourier decomposition into (3)-(4) yields an infinite system of equations for the mean flow $\overline{\mathbf{U}}$ and each coherent fluctuation $\widetilde{\mathbf{u}}_n$:

$$\mathbf{N}(\overline{\mathbf{U}}) = -\sum_{n \neq 0} \boldsymbol{\nabla} \cdot \widetilde{\mathbf{u}}_n \widetilde{\mathbf{u}}_{-n} - \boldsymbol{\nabla} \cdot \overline{\mathbf{u}'\mathbf{u}'}, \tag{8}$$

$$in\omega_1 \widetilde{\mathbf{u}}_n + \mathbf{L}(\overline{\mathbf{U}})\widetilde{\mathbf{u}}_n = -\sum_{m \neq n, 0} \boldsymbol{\nabla} \cdot \widetilde{\mathbf{u}}_m \widetilde{\mathbf{u}}_{n-m} - \boldsymbol{\nabla} \cdot (\widetilde{\mathbf{u}'\mathbf{u}'})_n + \delta_{n1} \widetilde{\mathbf{f}}_1, \tag{9}$$

where $(\widetilde{\mathbf{u}'\mathbf{u}'})_n$ denotes the coherent component at frequency $n\omega_1$ of the turbulent Reynolds stresses, and δ_{n1} is the Kronecker delta (equal to 1 if $n = 1$, and to 0 otherwise). For instance, the mean flow and first two harmonics are governed by

$$\mathbf{N}(\overline{\mathbf{U}}) = -(\widetilde{\boldsymbol{\psi}}_{1,-1} + \widetilde{\boldsymbol{\psi}}_{2,-2} \ldots) - \boldsymbol{\nabla} \cdot \overline{\mathbf{u}'\mathbf{u}'}, \tag{10}$$

$$(i\omega_1 + \mathbf{L}(\overline{\mathbf{U}}))\widetilde{\mathbf{u}}_1 = -(\widetilde{\boldsymbol{\psi}}_{2,-1} + \widetilde{\boldsymbol{\psi}}_{3,-2} \ldots) - \boldsymbol{\nabla} \cdot (\widetilde{\mathbf{u}'\mathbf{u}'})_1 + \widetilde{\mathbf{f}}_1, \tag{11}$$

$$(2i\omega_1 + \mathbf{L}(\overline{\mathbf{U}}))\widetilde{\mathbf{u}}_2 = -(\widetilde{\boldsymbol{\psi}}_{1,1} \quad + \widetilde{\boldsymbol{\psi}}_{3,-1} \ldots) - \boldsymbol{\nabla} \cdot (\widetilde{\mathbf{u}'\mathbf{u}'})_2, \tag{12}$$

where we have introduced the notations

$$\widetilde{\boldsymbol{\psi}}_{j,k} = \boldsymbol{\nabla}\cdot\widetilde{\mathbf{u}}_j\widetilde{\mathbf{u}}_k + c.c. \text{ if } j \neq k, \qquad \widetilde{\boldsymbol{\psi}}_{j,j} = \boldsymbol{\nabla}\cdot\widetilde{\mathbf{u}}_j\widetilde{\mathbf{u}}_j, \tag{13}$$

for the divergence of the coherent Reynolds stresses. At this stage, these equations are exact.

The effect of the unknown turbulent Reynolds stresses $\mathbf{u}'\mathbf{u}'$ on coherent fluctuations in (9) is accounted for with a turbulence model that relates $\widetilde{\mathbf{u}'\mathbf{u}'}$ to $\widetilde{\mathbf{u}}$ via a turbulent viscosity ν_t (see details in § 3.2), such that (11) becomes

$$(i\omega_1 + \mathbf{L}(\overline{\mathbf{U}}))\widetilde{\mathbf{u}}_1 = -(\widetilde{\boldsymbol{\psi}}_{2,-1} + \widetilde{\boldsymbol{\psi}}_{3,-2}\ldots) + \widetilde{\mathbf{f}}_1, \tag{14}$$

where $\mathbf{L}$ now contains the modified viscosity $\nu + \nu_t$.

We now make the central assumption that nonlinear forcing terms can be neglected (even though higher harmonics themselves may not be negligible), and that coherent fluctuations at ω_1 can be predicted by the linear response:

$$(i\omega_1 + \mathbf{L}(\overline{\mathbf{U}}))\widetilde{\mathbf{u}}_1 = \widetilde{\mathbf{f}}_1. \tag{15}$$

In the following, we will assess the ability of this simplified model to capture correctly amplification and saturation.

3.2 Numerical method

The two-dimensional linear response to time-harmonic forcing is calculated around the mean flow obtained from LES (§ 2). The LNSE (15) are recast in variational form and discretised in domain I with the finite-element software *FreeFem++* [Hecht, 2012], using P2 and P1 Taylor-Hood elements for velocity and pressure respectively ([Boujo et al., 2013, Boujo and Gallaire, 2015]). The two-dimensional mesh contains approximately 330 000 triangular elements, strongly clustered in the mixing layer. See Appendix A for a convergence study assessing the influence of the mesh size. Boundary conditions are as follows: $\widetilde{\mathbf{u}}_1 = \mathbf{0}$ at the inlet Γ_{in} and on the walls Γ_w, stress-free condition $\frac{1}{\rho}\widetilde{p}_1\mathbf{n} + (\nu + \nu_t)\widetilde{\mathbf{S}}_1 \cdot \mathbf{n} = 0$ at the outlet Γ_{out}, and spatially uniform vertical forcing $\widetilde{\mathbf{u}}_1 = v'\mathbf{e}_y$ at the cavity end Γ_f.

The effect of turbulent fluctuations is taken into account with a classical eddy viscosity model. The coherent component of the turbulent Reynolds stresses $\widetilde{\mathbf{u}'\mathbf{u}'}$ is assumed to be proportional to the coherent strain rate $\widetilde{\mathbf{S}} = \boldsymbol{\nabla}\widetilde{\mathbf{u}} + \boldsymbol{\nabla}\widetilde{\mathbf{u}}^T$ (Boussinesq approximation):

$$\widetilde{\mathbf{u}'\mathbf{u}'} - \frac{2}{3}\widetilde{q}\mathbf{I} = -2\nu_t\widetilde{\mathbf{S}}, \tag{16}$$

where $\widetilde{q} = \widetilde{\mathbf{u}' \cdot \mathbf{u}'}/2$ is the kinetic energy and $\mathbf{I}$ the identity tensor. In this study the turbulent viscosity ν_t is taken as space dependent, and calculated at each location according to

$$\nu_t(\mathbf{x}) = -\frac{\overline{\mathbf{u}'\mathbf{u}'} : \overline{\mathbf{S}}}{2\overline{\mathbf{S}} : \overline{\mathbf{S}}}, \tag{17}$$

where $:$ denotes the Frobenius inner product. (In other words, at each location ν_t can be seen as resulting from the least-square minimisation of the over-determined system of equations $\overline{\mathbf{u}'\mathbf{u}'} = -2\nu_t\overline{\mathbf{S}}$.) The steady component of the turbulent Reynolds stresses $\overline{\mathbf{u}'\mathbf{u}'}$ and the mean strain rate $\overline{\mathbf{S}} = \boldsymbol{\nabla}\overline{\mathbf{U}} + \boldsymbol{\nabla}\overline{\mathbf{U}}^T$ are evaluated from the LES.

As mentioned in Pope [Pope, 2000], the above model is a two-fold simplification: *“First, there is the intrinsic assumption that (at each point and time) the Reynolds-stress anisotropy*

$\widetilde{\mathbf{u}'\mathbf{u}'} - \frac{2}{3}\widetilde{q}\mathbf{I}$ *is determined by the mean velocity gradients. Second, there is the specific assumption that the relationship (...) is (16). This is, of course, directly analogous to the relation for the viscous stress in a Newtonian fluid. (...) In general, the turbulent viscosity hypothesis is incorrect. These general objections notwithstanding, there are important particular flows for which the hypothesis is more reasonable. In simple turbulent shear flows (e.g., the round jet, mixing layer, channel flow, and boundary layer) the turbulence characteristics and mean velocity gradients change relatively slowly (following the mean flow). As a consequence, the local mean velocity gradients characterise the history of the mean distortion to which the turbulence has been subjected; and the Reynolds-stress balance is dominated by local processes (...), the non-local transport processes being small in comparison. In these circumstances, then, it is more reasonable to hypothesise that there is a relationship between the Reynolds stresses and the local mean velocity gradients."*

It should be noted that, in (17), $\overline{\mathbf{S}}$ is a direct output of the LES, whereas the calculation of $\overline{\mathbf{u}'\mathbf{u}'}$ requires further processing: indeed, the total statistics of the velocity field contain the steady component of both turbulent and coherent Reynolds stresses $\overline{\mathbf{u}'\mathbf{u}'} + \overline{\widetilde{\mathbf{u}}\widetilde{\mathbf{u}}}$. This can be overlooked if the stresses $\overline{\widetilde{\mathbf{u}}\widetilde{\mathbf{u}}}$ are small compared to $\overline{\mathbf{u}'\mathbf{u}'}$ ([Kitsios et al., 2010, Viola et al., 2014]), which is not the case here because substantial coherent fluctuations are produced by the harmonic forcing in the large-amplitude regime. Therefore, before computing the turbulent viscosity, we first remove the coherent contribution $\overline{\widetilde{\mathbf{u}}_1\widetilde{\mathbf{u}}_{-1}}$ at the fundamental frequency, with $\widetilde{\mathbf{u}}_{\pm 1}$ obtained from frequency analysis. Some authors have used an alternative approach based on energetic structures obtained from proper orthogonal decomposition ([Tammisola and Juniper, 2016]) or have proposed weighting the turbulent viscosity by a laminar-turbulent intermittency factor ([Oberleithner et al., 2014]).

3.3 Unforced case: linear stability analysis and linear harmonic response

We first focus on the unforced case, $v' = 0$. Before moving to the harmonic response problem, we investigate linear stability by solving the eigenvalue problem

$$(\sigma + i\omega)\widetilde{\mathbf{u}} + \mathbf{L}(\overline{\mathbf{U}})\widetilde{\mathbf{u}} = \mathbf{0} \tag{18}$$

for infinitesimal perturbations $\widetilde{\mathbf{u}}$ around the LES mean flow $\overline{\mathbf{U}}$, with the numerical method as described in § 3.2. As shown in the spectrum in figure 3(a), all eigenmodes are stable (growth rate $\sigma \leq 0$). Most eigenvalues fall on continuous branches, and are more stable at larger frequencies. Two eigenmodes (denoted 1 and 2) stand out, however, at frequencies close to 750 and 1000 Hz, and are marginally stable (small growth rate compared to the angular frequency, $|\sigma| \ll \omega$). Marginal stability in mean flows has been observed in some laminar and turbulent flows, as well as counter-examples ([Barkley, 2006, Sipp and Lebedev, 2007, Turton et al., 2015, Meliga, 2017]). Modes 1 and 2 are located in the shear layer and the downstream boundary layer, and exhibit approximately one and two wavelengths across the cavity, respectively, as shown in fig. 3($b1, b2$). Other modes are located inside the cavity, e.g. mode 3 in fig. 3($b3$). Discarding turbulent viscosity in the linear stability analysis (i.e. in $\mathbf{L}$ in the eigenvalue problem (18)) does not affect substantially eigenvalues 1 and 2 (black crosses in panel a), and has a limited impact on the structure of modes 1 and 2 in the shear layer (panels $c1$, $c2$).

Next, the linear response of the mean unforced flow to harmonic forcing on Γ_f is characterised in terms of kinetic energy in domain I with the gain

$$G(\omega) = \frac{1}{v'} \left(\iint_{\mathrm{I}} |\widetilde{\mathbf{u}}_1|^2 \, \mathbf{dx} \right)^{1/2}. \tag{19}$$

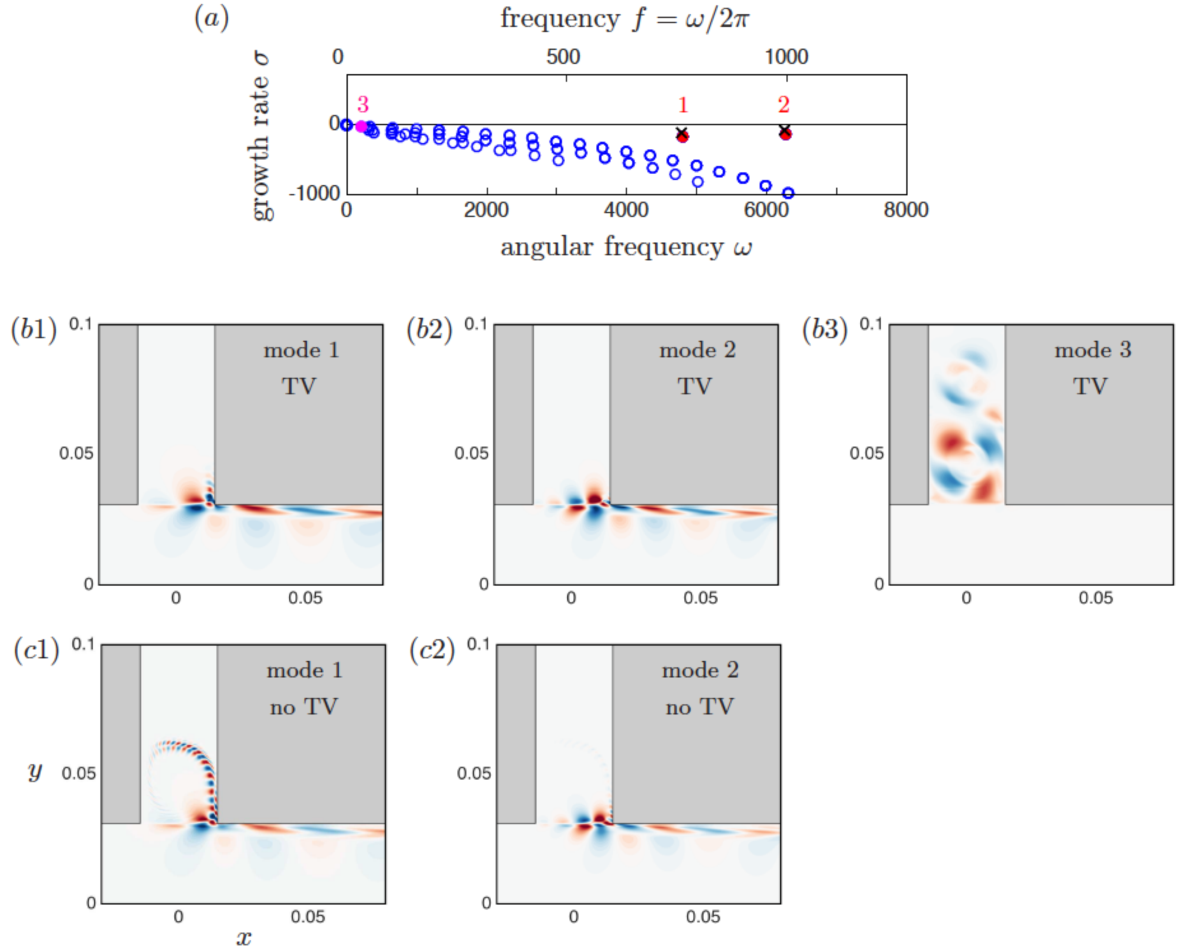

Figure 3: Global linear stability around the unforced mean flow ($v' = 0$). (a) Eigenvalues lie on continuous branches, except marginally stable eigenvalues 1 and 2 which stand out at $\omega/2\pi = 750$ and 1000 Hz. These two eigenvalues are not substantially affected by discarding turbulent viscosity (crosses). (b, c) Eigenmodes (streamwise component, real part). Modes 1 and 2 are located in the shear layer and the downstream boundary layer, computed either with turbulent viscosity ("TV", panels $b1$, $b2$) or without ("no TV", panels $c1$, $c2$). ($b3$) Other modes are located inside the cavity.

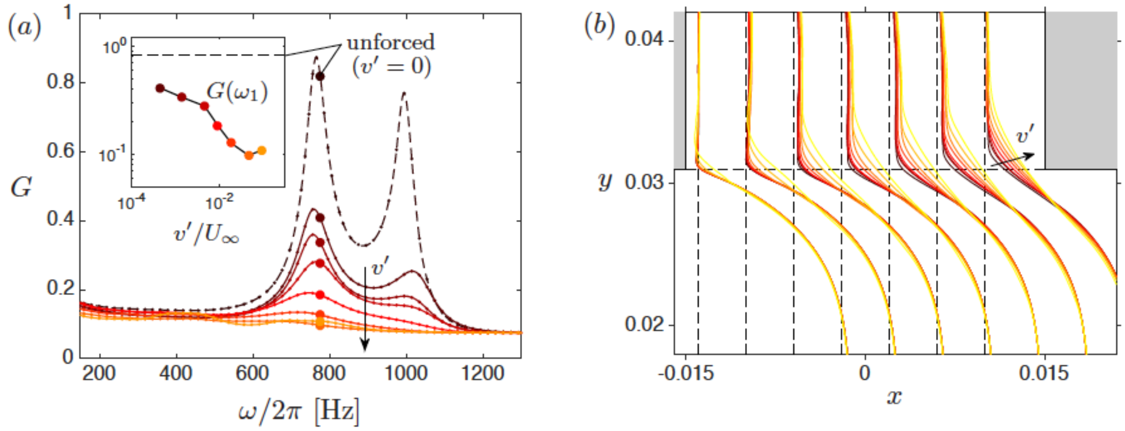

Figure 4: (a) Linear harmonic gain $G(\omega)$ of the turbulent mean flow forced at $\omega_1/2\pi = 750$ Hz at different amplitudes v'. Inset: $G(\omega_1)$ in logarithmic scale. (b) Profiles of mean streamwise velocity $\overline{U}$.

Figure 4(a) shows the gain obtained from the LNSE over a broad range of forcing frequencies (dashed line). The forcing is amplified preferentially in the frequency range 600-1200 Hz, with clear peaks close to 750 and 1000 Hz that can be related to the marginally stable modes 1 and 2.

3.4 Forced cases, saturation of the linear harmonic response

We now turn our attention to mean flows obtained from LES with harmonic forcing at $\omega_1/2\pi = 750$ Hz, and recompute the linear response to harmonic forcing. In these mean flows, the gain consistently decreases with the forcing amplitude (solid lines in fig. 4a).

In the following, we focus on the linear response to harmonic forcing at the frequency ω_1 of the dominant peak. At this specific frequency (inset), the gain decreases by approximately one order of magnitude from the unforced regime to the large-amplitude forcing regime $v' \gtrsim 2.5$ m/s. It should be noted that this effect comes entirely from the mean flow, which varies with v'. Specifically, the mixing layer becomes thicker as v' increases (fig. 4b), suggesting that the weaker shear is the main cause for the reduced amplification.

Next, we take a closer look at the rectangular subdomain $\mathrm{J} = \{(x,y)| -W/2 \leq x \leq W/2, 0 \leq y\}$ spanning exactly the streamwise extension of the cavity. Figure 5(a) compares the harmonic gain restricted to region J, obtained from LES and LNSE at ω_1:

$$\frac{1}{v'}\left(\iint_{\mathrm{J}} |\tilde{\mathbf{u}}_1|^2 \,\mathbf{dx}\right)^{1/2}. \tag{20}$$

The overall agreement is very good, with LNSE capturing well the decrease in gain observed in the LES. The slight discrepancy at very low forcing amplitude ($v' = 0.025$ m/s) can be ascribed to the small signal-to-noise ratio in the LES, which makes it difficult to to measure the gain accurately. In the large-amplitude forcing regime, LNSE overestimates the coherent response, which points to non-negligible contributions from higher harmonics and/or to a deteriorating turbulent viscosity model. The inset illustrates the saturation of the response itself (prior to normalisation by v'), with the slope quickly departing from the LNSE result obtained with the unforced flow (dashed line).

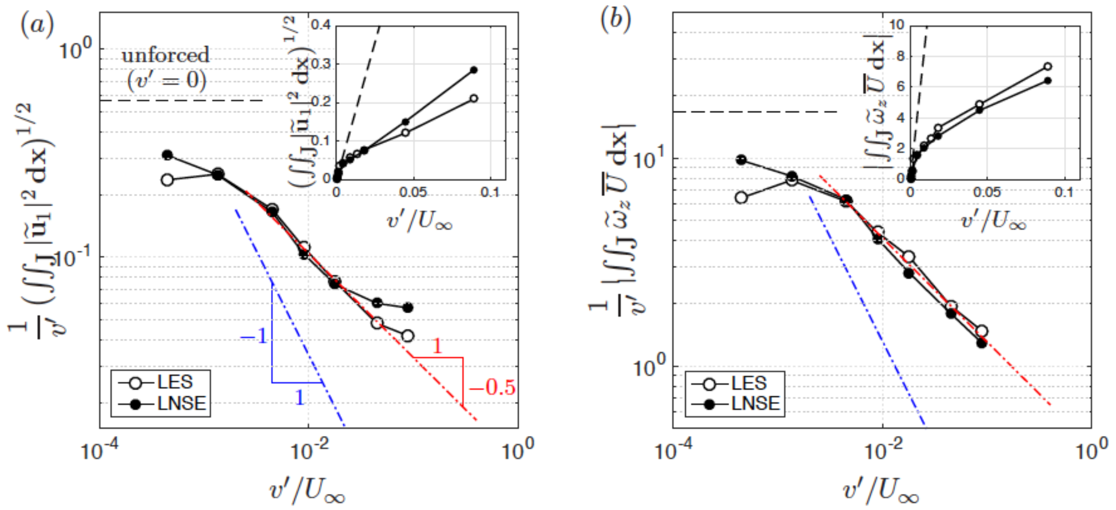

Figure 5: Harmonic gain (logarithmic scale) at $\omega_1/2\pi = 750$ Hz vs. forcing amplitude, from LES (open symbols) and LNSE (filled symbols). The gain is calculated with the response measured in terms of (*a*) kinetic energy (20) and (*b*) dominant contribution of the vertical component of the unsteady Coriolis force (21). The linear gain for the unforced flow ($v' = 0$) is shown as a horizontal dashed line. Also shown are the slope -0.5 (red) that fits the data for $v'/U_\infty \geq 0.45\%$, and the slope -1 (blue) that would be obtained for full saturation. Insets: harmonic response (linear scale).

Figure 5(*b*) shows an alternative measure of the gain, useful in an aeroacoustic context: we define

$$\frac{1}{v'} \left| \iint_{\mathbf{J}} \widetilde{\omega}_z \, \overline{U} \, \mathbf{dx} \right|, \tag{21}$$

where $\widetilde{\omega}_z = \partial_x \widetilde{v} - \partial_y \widetilde{u}$ is the spanwise vorticity of the coherent response. This measure gives insight into vortex sound production, since the Coriolis force $\mathbf{\Omega} \times \mathbf{U}$ is related to the acoustic power $\mathcal{P}$ of a low-Mach number compact vorticity distribution, as expressed for instance by Howe's formula [Howe, 1980]

$$\mathcal{P} = - \iint \overline{\rho} (\mathbf{\Omega} \times \mathbf{U}) \cdot \mathbf{u}_{ac} \, \mathbf{dx}, \tag{22}$$

where $\mathbf{U}$ is the total unsteady velocity field, $\mathbf{\Omega}$ the total vorticity field, and $\mathbf{u}_{ac}$ the acoustic (irrotational) component of the fluctuation. In the present configuration, the above expression is well approximated by the contributions from the vertical component v_{ac} of the acoustic fluctuations and from the vertical component $\Omega_z U$ of the Coriolis force. In addition, the dominant contribution to the time-averaged power comes from $\widetilde{\omega}_z \overline{U}$, hence our choice for (21). (See [Bauerheim et al., 2017] for an in-depth analysis and discussion.) Here again, the agreement between LES and LNSE results is very good, which suggests that the linearised approach can provide useful quantitative estimates of the produced acoustic power.

Both gains (20) and (21) decrease like $\sim 1/\sqrt{v'}$, as shown by the red line of slope -0.5. This is weaker than full saturation, which would yield $\sim 1/v'$ (blue line of slope -1), i.e. a response not increasing at all when the forcing amplitude increases. [Graf and Ziada, 2010] and [Nakiboğlu et al., 2012] reported a similar saturation slope of approximately -0.6 in other cavity flows (deep circular cavity $W/H = 0.08$ and shallow axisymmetric cavity $W/H = 1.48$, respectively).

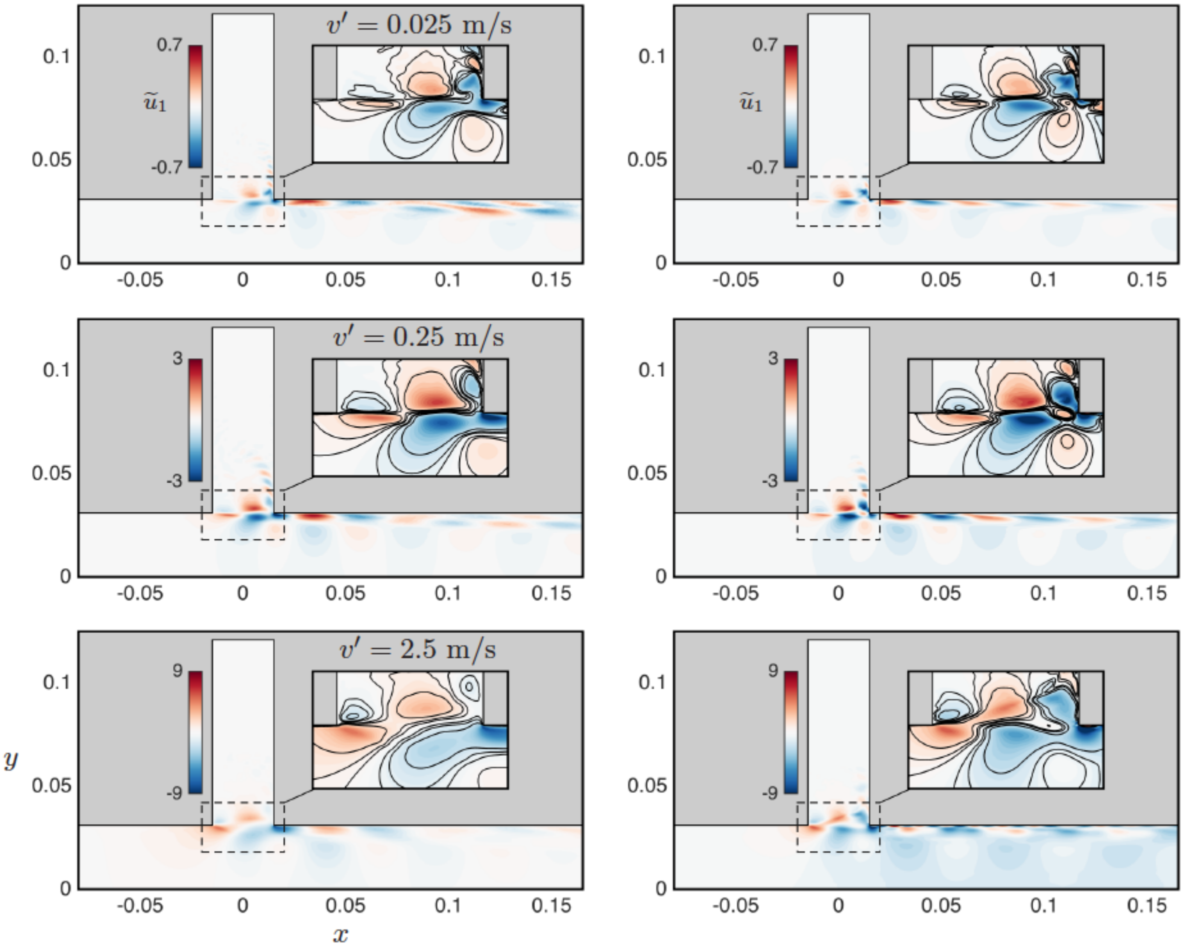

Figure 6: Streamwise component of $\widetilde{\mathbf{u}}_1$ at ω_1. Left: LES spectral component. Right: LNSE linear harmonic response around the mean flow. Forcing amplitudes $v' = 0.025$, 0.25 and 2.5 m/s.

The spatial structure of the harmonic response at ω_1 is shown in figure 6, obtained from the LNSE calculation and from a spectral decomposition of the LES. The response is localised in the mixing layer, and in the downstream boundary layer. At low and medium forcing amplitudes, it has a distinct wave packet structure and experiences a clear streamwise growth, with weak perturbations generated close to the upstream corner and amplified while convected by the mean flow to the downstream corner. This is typical of the linear response or instability of mixing layers. At larger forcing amplitudes, the wave packet structure is less well organised and perturbations are convected with no substantial growth. At this frequency, one wavelength of the coherent response (i.e. one vortical structure) almost exactly fills the cavity width. The shape and amplitude of the responses obtained from LNSE and LES are very similar, except in the vicinity of the downstream corner and for the largest forcing amplitudes.

Figure 7 and 8 show snapshots of the response obtained from LES and LNSE at four time instants of an oscillation cycle separated by $T_1/4$, with $T_1 = 2\pi/\omega_1$ the forcing period. At small forcing amplitude (panels *a* and *c*), the gain is larger than at other forcing amplitudes but the resulting coherent response is small compared to the mean flow, and oscillations in the total flow are barely distinguishable. Snapshots of streamwise velocity and spanwise vorticity depict the formation and advection of two main vortical structures of opposite vorticity in the first and second half-periods. At larger forcing amplitude (panels *b* and *d*), the amplification is substantially smaller but the coherent response is large enough that fluctuations in the total flow are visible. One can clearly observe the role of the upstream corner in the formation of vortical structures, with $\omega_z > 0$ when the forcing is directed upward (toward the cavity end) and, $T_1/2$ later, $\omega_z < 0$ when the forcing is directed downward (toward the main channel).

As observed in figures 6-7, the location of strongest response, where $\widetilde{\mathbf{u}}_1$ is maximal, moves upstream as the forcing amplitude $|v'|$ increases. This is further quantified in figure 9, which represents the streamwise evolution of the coherent kinetic energy integrated vertically in J ($y > 0$), i.e. the coherent energy density

$$E_y(x) = \int_{y>0} E(x,y)\,\mathrm{d}y = \frac{1}{2}\int_{y>0} |\widetilde{u}_1|^2 + |\widetilde{v}_1|^2\,\mathrm{d}y. \tag{23}$$

At low forcing amplitudes, E_y increases exponentially with x, consistent with the streamwise amplification mentioned earlier and with a linear amplification scenario, and reaches its maximum close to the downstream corner. As the forcing amplitude increases, the region of exponential amplification becomes shorter and eventually vanishes; consequently, E_y reaches its maximum already near the middle of the cavity, and eventually even in the first half.

This upstream migration can be understood in terms of the mean flow distortion induced by the Reynolds stresses. As mentioned in § 3, the mean flow is forced by Reynolds stress divergence terms (see e.g. (3)). As the forcing amplitude increases, coherent Reynolds stresses build up earlier upstream (figure 10), leading to a thickening of the mean shear layer. In turn, the coherent response building up around this increasingly diffused mean flow benefit from a reduced potential for amplification, and saturate earlier upstream. This segregated yet coupled description, i.e. the interaction between (i) the nonlinear mean flow forced by the coherent response and (ii) the linear monochromatic coherent response around the mean flow, is the central ingredient of the simplified self-consistent model proposed to predict the saturation mechanism at play under harmonic forcing [Mantič-Lugo and Gallaire, 2016].

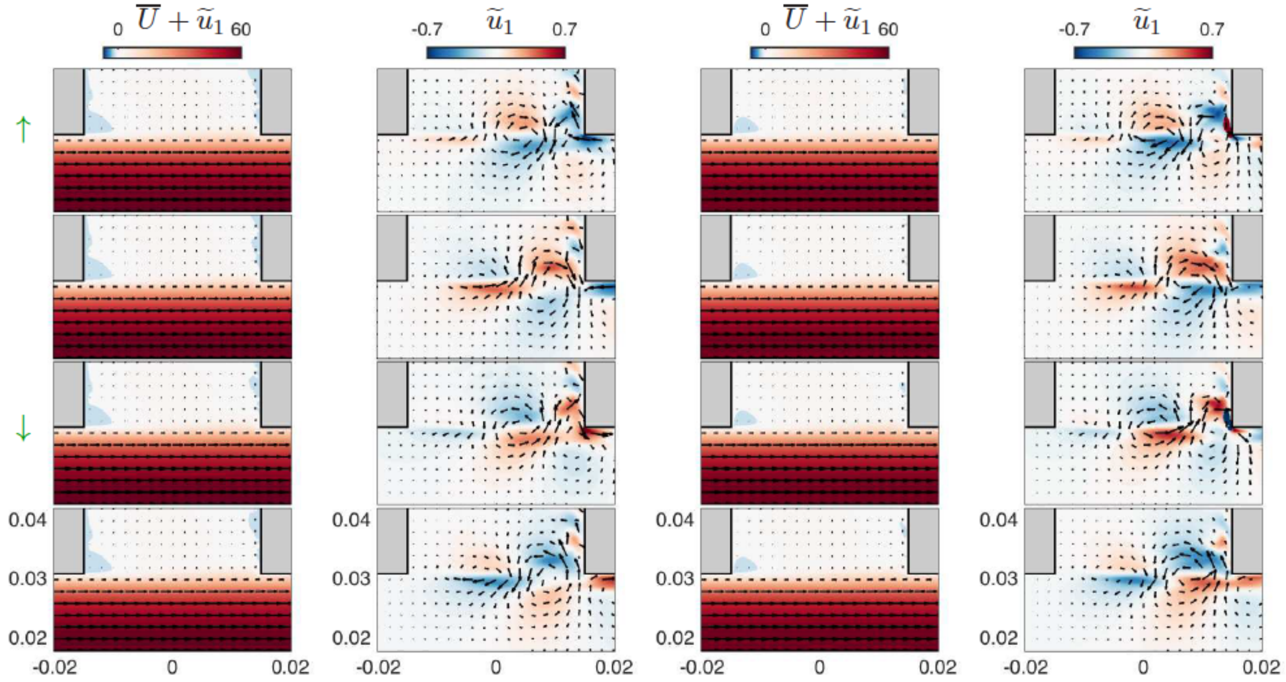

(a) LES, $v' = 0.025$ m/s

(c) LNSE, $v' = 0.025$ m/s

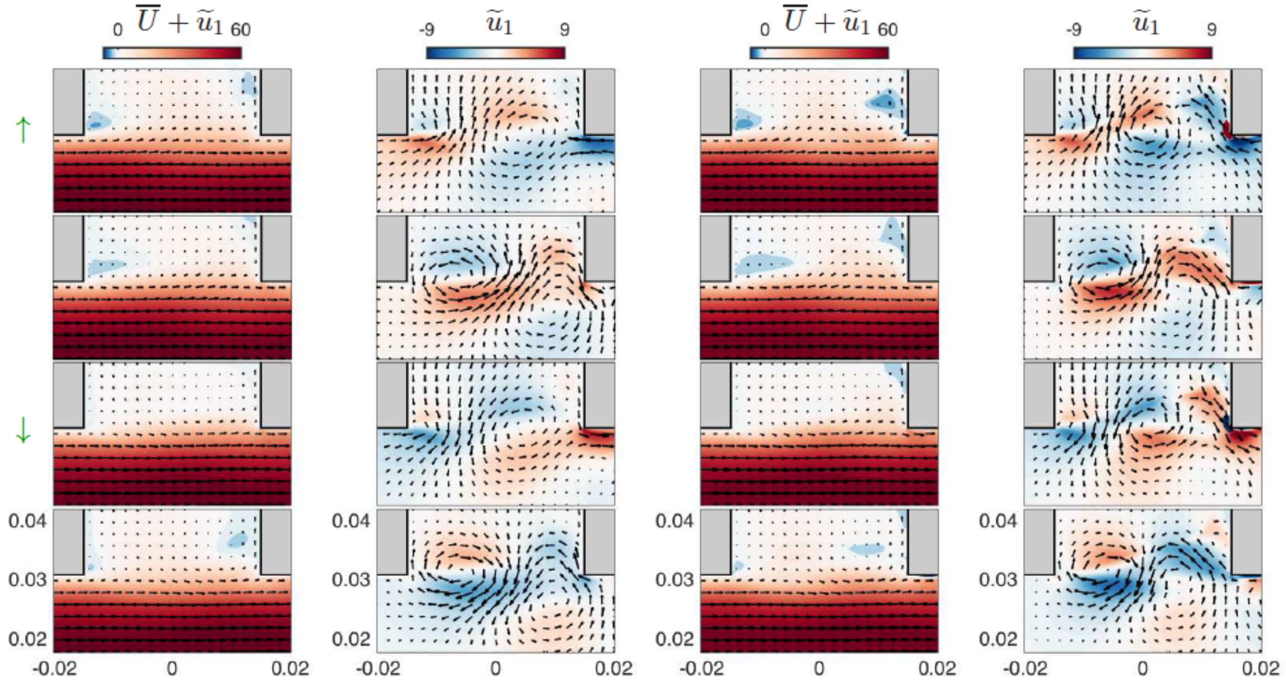

(b) LES, $v' = 2.5$ m/s

(d) LNSE, $v' = 2.5$ m/s

Figure 7: Contours of streamwise velocity: phase-averaged velocity $\overline{U}+\widetilde{u}_1$ and coherent velocity fluctuations $\widetilde{u}_1$. (Overlaid are arrows of the phase-averaged and coherent fluctuating velocity fields $\overline{\mathbf{U}}+\widetilde{\mathbf{u}}_1$ and $\widetilde{\mathbf{u}}_1$, respectively.) (a,b) LES, (c,d) LNSE. Forcing amplitudes: (a,c) $v' = 0.025$ m/s, (b,d) $v' = 2.5$ m/s. Time instants in each panel, from top to bottom: t (forcing directed upward ↑), $t+T_1/4$, $t+T_1/2$ (forcing directed downward ↓) and $t+3T_1/4$.

(a) LES, $v' = 0.025$ m/s

(c) LNSE, $v' = 0.025$ m/s

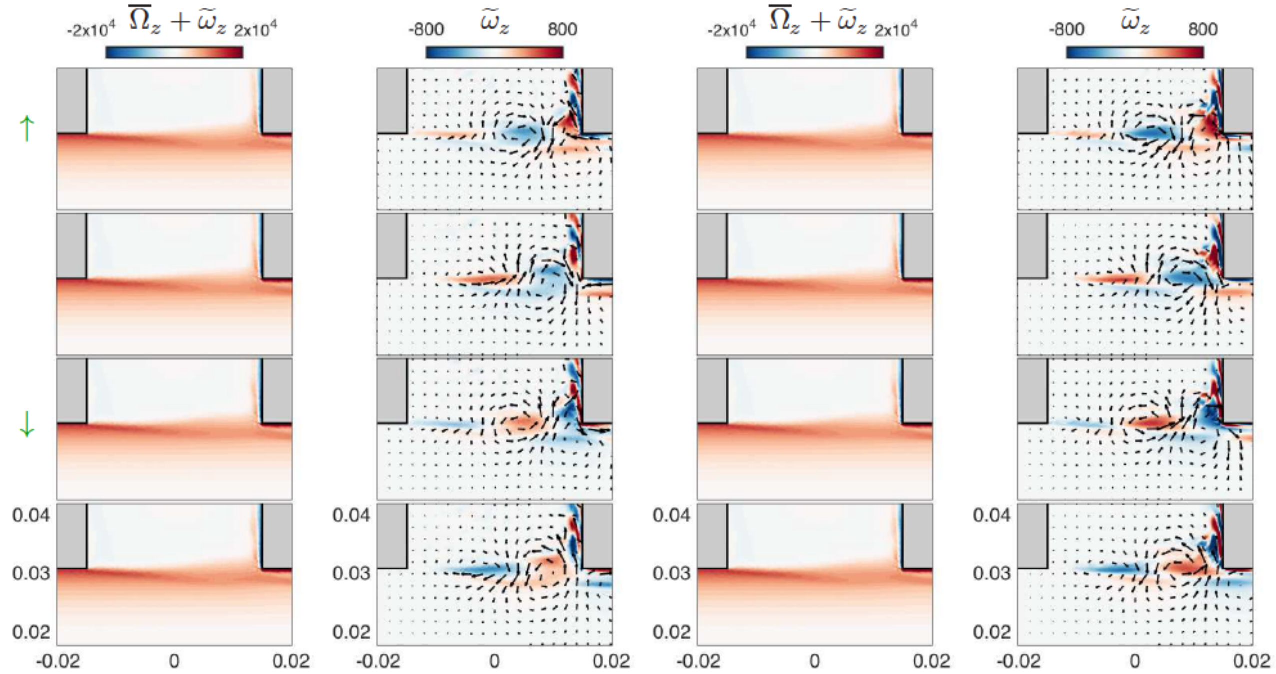

(b) LES, $v' = 2.5$ m/s

(d) LNSE, $v' = 2.5$ m/s

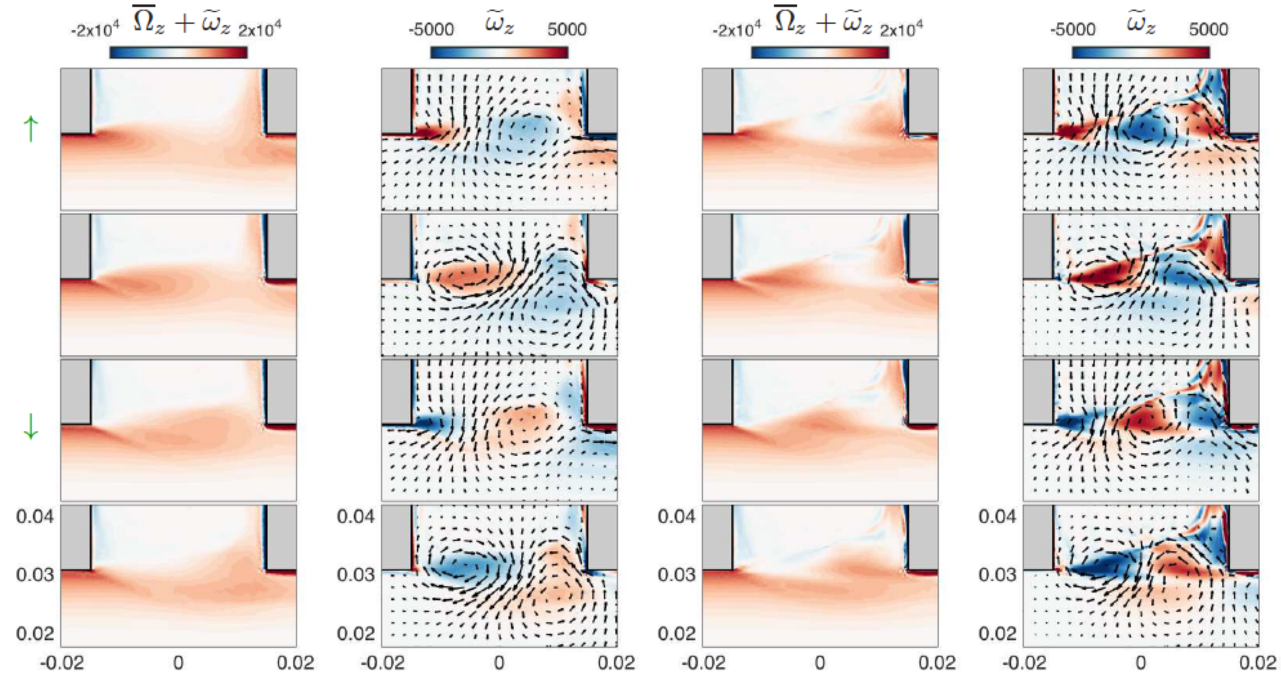

Figure 8: Contours of spanwise vorticity: phase-averaged vorticity $\overline{\Omega}_z + \widetilde{\omega}_z$ and coherent vorticity fluctuations $\widetilde{\omega}_z$. (Overlaid are arrows of the coherent fluctuating velocity field $\widetilde{\mathbf{u}}_1$.) (a, b) LES, (c, d) LNSE. Forcing amplitudes: (a, c) $v' = 0.025$ m/s, (b, d) $v' = 2.5$ m/s. Time instants in each panel, from top to bottom: t (forcing directed upward ↑), $t + T_1/4$, $t + T_1/2$ (forcing directed downward ↓) and $t + 3T_1/4$.

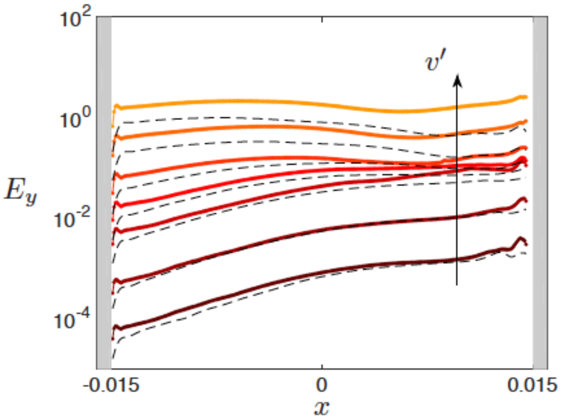

Figure 9: Streamwise evolution of the energy density (23). Thick solid lines: LNSE harmonic response; Thin dashed lines: LES spectral component.

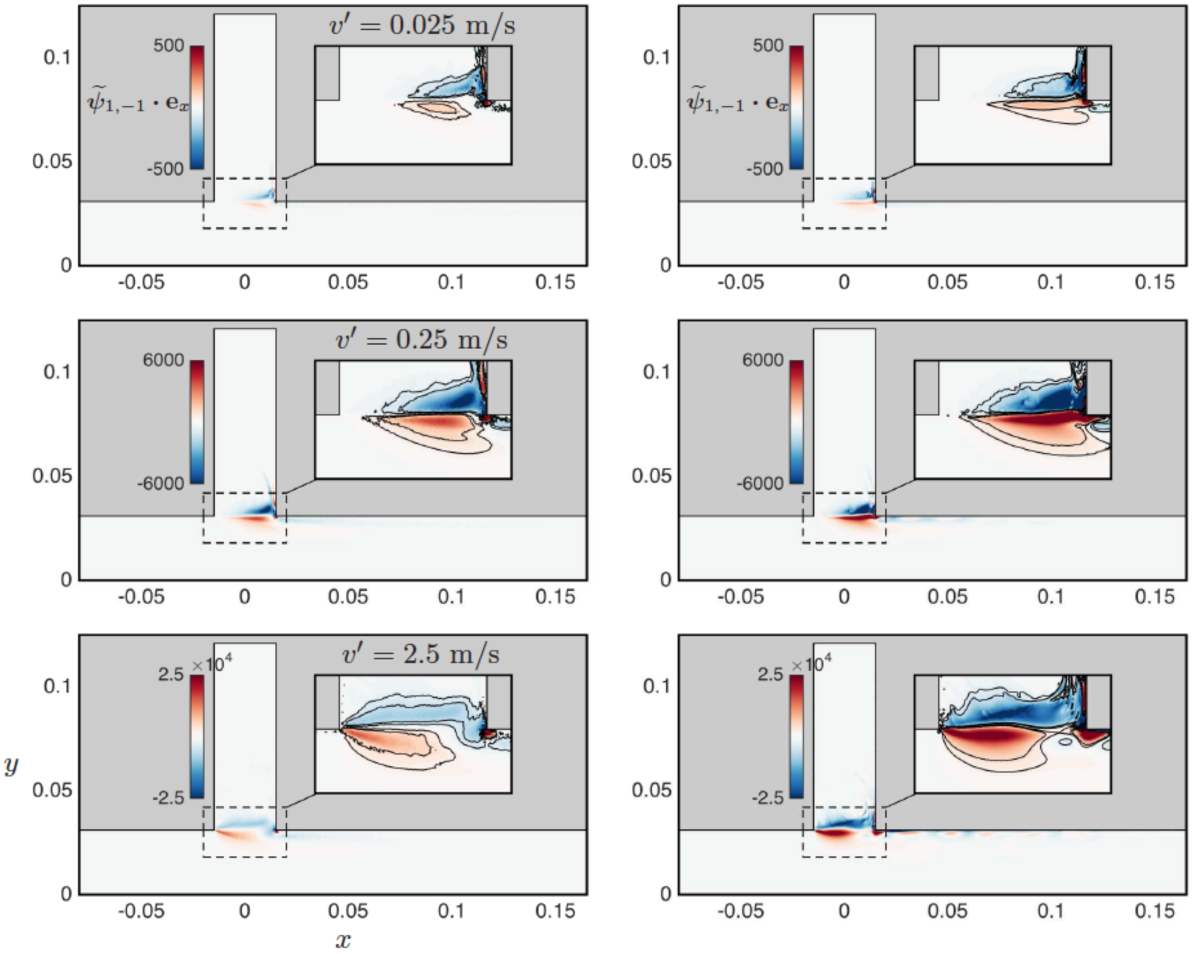

Figure 10: Divergence of the coherent Reynolds stress, $\widetilde{\boldsymbol{\psi}}_{1,-1}$ (vertical component), acting as a forcing term for the mean flow (see (10)). Left: LES; right: LNSE. Forcing at ω_1, amplitudes $v' = 0.025$, 0.25 and 2.5 m/s.

4 Validity of the monochromatic approximation

4.1 Amplitude of higher harmonics and corresponding forcing terms

In the previous section we have considered the linear response at only one frequency, equal to the forcing frequency ω_1, and we have focused on the external forcing $\widetilde{\mathbf{f}}_1$, neglecting other forcing terms arising at ω_1 from the interaction of higher-frequency coherent fluctuations, i.e. Reynolds stress divergence terms $\widetilde{\boldsymbol{\psi}}_{j,1-j}$, $j \geq 2$, in (14). The good agreement found between the response obtained in this LNSE framework and the flow computed with a fully nonlinear LES suggests that the nonlinear interaction of higher harmonics plays a negligible role on the response. (Note that this still requires the correct mean flow $\overline{\mathbf{U}}$, which is crucially determined by $\widetilde{\boldsymbol{\psi}}_{1,-1}$ and possibly influenced by higher-order terms $\widetilde{\boldsymbol{\psi}}_{j,-j}$ as well. Here we use the fully nonlinear LES mean flow; a predictive method doing without direct nonlinear simulations would have to account for these Reynolds stresses carefully.) In the following, we investigate this aspect further.

In general, if higher harmonics are small, their interaction is necessarily small too. We note that, in the present flow, the second harmonic $\widetilde{\mathbf{u}}_2$ (extracted from the LES at $\omega_2 = 2\omega_1$) is smaller than $\widetilde{\mathbf{u}}_1$ but far from negligible: the ratio $||\widetilde{\mathbf{u}}_1||/||\widetilde{\mathbf{u}}_2||$ is less than one order of magnitude (figure 11*a*). In [Turton et al., 2015], linear stability analysis around the mean flow in a laminar thermosolutal convection system reproduced well nonlinear characteristics for traveling waves whereas it failed for standing waves, which was explained by a negligible (resp. non-negligible) second harmonic in the former (resp. latter) case.

Higher harmonics, albeit not negligible, may still contribute only marginally to the harmonic response at ω_1, either (i) if their interaction as Reynolds stress divergence $\widetilde{\boldsymbol{\psi}}_{j,1-j}$ is small, or (ii) if the response to these forcing terms is small. Regarding condition (i), it would be natural to quantify rigorously what "small $\widetilde{\boldsymbol{\psi}}_{j,1-j}$" means by comparing these forcing terms to the external forcing $\widetilde{\mathbf{f}}_1$; however, this not possible in the present configuration since the $\widetilde{\boldsymbol{\psi}}_{j,1-j}$ are defined in the volume while $\widetilde{\mathbf{f}}_1$ is applied at a boundary. Nonetheless, we report for the sake of completeness the norm of $\widetilde{\boldsymbol{\psi}}_{2,-1}$, the first (and likely dominant) Reynolds stress divergence term, in figure 11(*b*). Regarding condition (ii), which may be verified irrespective of condition (i), comparing the response to each forcing term is straightforward; the question is therefore whether the response to the (possibly non-small) Reynolds stress forcing is small compared to the response $\widetilde{\mathbf{u}}_1$ to the external forcing:

$$(i\omega_1 + \mathbf{L}(\overline{\mathbf{U}}))^{-1}\widetilde{\boldsymbol{\psi}}_{j,1-j} \ll (i\omega_1 + \mathbf{L}(\overline{\mathbf{U}}))^{-1}\widetilde{\mathbf{f}}_1\,? \tag{24}$$

Figure 11(*a*) reports the norm of $\check{\mathbf{u}}_1 = (i\omega_1 + \mathbf{L}(\overline{\mathbf{U}}))\widetilde{\boldsymbol{\psi}}_{2,-1}$. At the two lowest forcing amplitudes, $\check{\mathbf{u}}_1$ is indeed much smaller than $\widetilde{\mathbf{u}}_1$ (in excess of 20 and 5 times, respectively). At larger amplitudes, however, both responses are of the same order of magnitude. At first glance, this seems at odds with the fact that $\widetilde{\mathbf{u}}_1$ alone is sufficient to predict the overall coherent fluctuations at ω_1. Interestingly, a closer look reveals that $\check{\mathbf{u}}_1$ and $\widetilde{\mathbf{u}}_1$ have different phases and therefore cannot interact constructively, meaning that the norm of the response is essentially unaffected by $\check{\mathbf{u}}_1$.

4.2 Optimal response: harnessing the potential for amplification

Further insight is gained by quantifying how efficiently the two forcing terms (external forcing, and forcing from the interaction of higher harmonics) are amplified. A direct comparison of the gains $||\widetilde{\mathbf{u}}_1||/||\widetilde{\mathbf{f}}_1||$ and $||\check{\mathbf{u}}_1||/||\widetilde{\boldsymbol{\psi}}_{2,-1}||$ gives little information, because the forcing terms

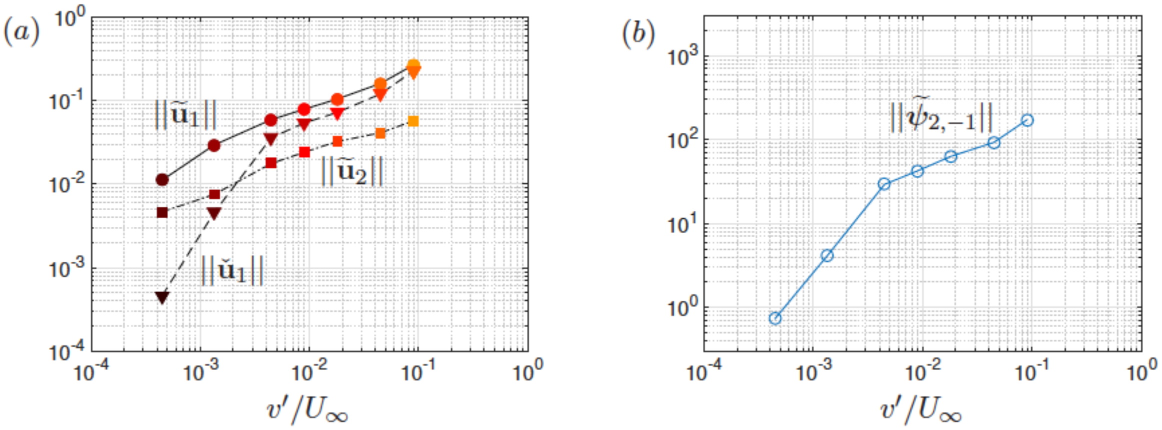

Figure 11: (*a*) Norm of the higher harmonic $\widetilde{\mathbf{u}}_2$ at $2\omega_1$ (LES), of the response $\widetilde{\mathbf{u}}_1$ to the external forcing $\widetilde{\mathbf{f}}_1$ at ω_1 (LES), and of the response $\check{\mathbf{u}}_1$ to the first Reynolds stress divergence forcing term $\widetilde{\boldsymbol{\psi}}_{2,-1}$ at ω_1 (LNSE). (*b*) Norm of $\widetilde{\boldsymbol{\psi}}_{2,-1}$.

are defined on a boundary and in the domain, respectively. However, it is possible to assess whether each forcing efficiently exploits the potential for amplification available in the flow. In this context, it is natural to introduce the concept of optimal gain, which corresponds to the largest possible linear amplification in the flow at a given frequency: instead of solving

$$(i\omega + \mathbf{L}(\overline{\mathbf{U}}))\mathbf{u} = \mathbf{f} \tag{25}$$

to compute the linear response $\mathbf{u}$ to a *given* harmonic forcing $\mathbf{f}$ (defined either on a boundary or in the domain), the idea is to identify the *optimal* forcing $\mathbf{f}^{(opt)}$ which maximises the gain

$$G^{(opt)}(\omega) = \max_{\mathbf{f}} \frac{||\mathbf{u}||}{||\mathbf{f}||} = \frac{||\mathbf{u}^{(opt)}||}{||\mathbf{f}^{(opt)}||}. \tag{26}$$

The optimal gain is obtained by performing a singular value decomposition of the resolvent operator defined by

$$\mathbf{u} = (i\omega + \mathbf{L}(\overline{\mathbf{U}}))^{-1}\mathbf{f} = \mathbf{R}(\omega)\mathbf{f}, \tag{27}$$

or, equivalently, by solving the eigenvalue problem $\mathbf{R}^\dagger\mathbf{R}\mathbf{f} = G^2\mathbf{f}$ (where $\mathbf{R}^\dagger$ is the adjoint resolvent operator). If needed, the calculation actually yields more, namely an orthogonal set of optimal forcings $\mathbf{f}^{(k)}$ and the corresponding set of optimal responses $\mathbf{u}^{(k)}$ associated with optimal gains $G^{(k)}$ sorted in decreasing order:

$$G^{(opt)} = G^{(1)} \geq G^{(2)} \geq G^{(3)} \dots \tag{28}$$

Examples of resolvent analyses around turbulent mean flows include [Farrell and Ioannou, 1993, McKeon et al., 2013, Garnaud et al., 2013, Beneddine et al., 2016].

Figure 12 shows the first three optimal gains for harmonic forcing applied at ω_1 at the cavity end or in the domain. At small forcing amplitudes, the first optimal gain is more than one order of magnitude larger than the following optimal gains, which has been observed in other flows ([Dergham et al., 2013, Boujo and Gallaire, 2015, Beneddine et al., 2016]). At larger amplitudes, this clear separation persists for boundary forcing, while for volume forcing the first optimal forcing becomes increasingly less amplified and is eventually comparable to the following optimal forcings.

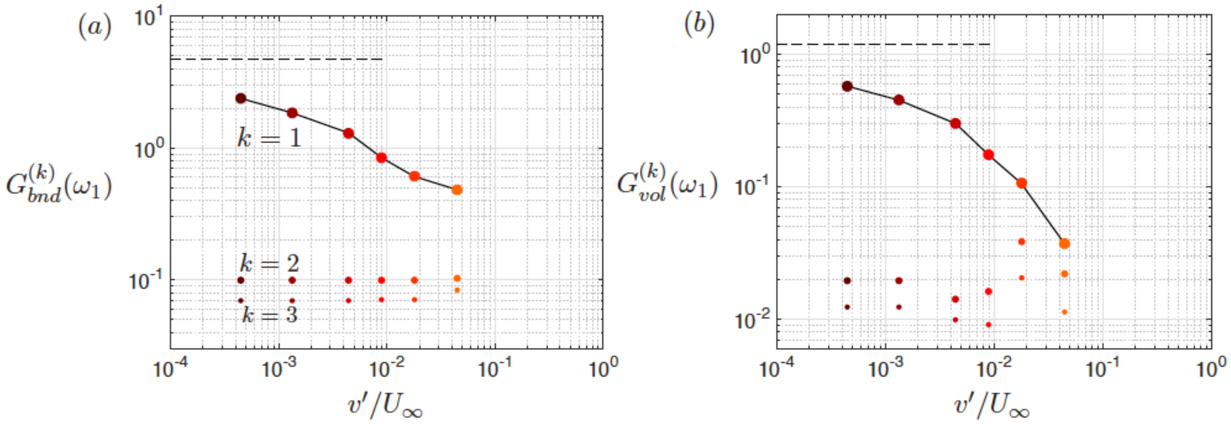

Figure 12: First three optimal gains at ω_1, for (a) boundary forcing at the cavity end Γ_f, or (b) volume forcing in the domain I.

In both cases, the first optimal gain decreases with forcing amplitude, indicating that the dominant amplification mechanism weakens as the mean flow is modified. This is confirmed by the optimal volume forcing and optimal response shown in figure 13: they clearly identify the mixing layer as the main amplification region, and shear as the main amplification mechanism.

The first three optimal boundary forcings at the cavity end Γ_f are shown in figure 14 for $v' = 0.075$ m/s (they are essentially independent of v'). They exhibit an increasing number of spatial oscillations over the cavity width. Interestingly, the first optimal is uniform, meaning that the external forcing $\widetilde{\mathbf{f}}_1$ considered in this study is actually optimal. The response to the optimal boundary forcing has therefore the same structure as the response to $\widetilde{\mathbf{f}}_1$ shown in figure 6. One can observe that the optimal volume response and optimal boundary response have very similar structures at lower and intermediate forcing amplitudes, i.e. when the first optimal gain is much larger than the following optimal gains.

One might wonder whether the volume forcing term from the Reynolds stress divergence $\widetilde{\boldsymbol{\psi}}_{2,-1}$ is close to the optimal volume forcing. For a quantitative answer, let us decompose any forcing $\mathbf{f}$ (at a boundary or in the domain) using the optimal forcings ($\mathbf{f}^{(k)}_{bnd}$ or $\mathbf{f}^{(k)}_{vol}$):

$$\mathbf{f} = \sum_{k\geq 1} \alpha^{(k)} \mathbf{f}^{(k)}. \tag{29}$$

Since the optimal forcings are orthogonal, the coefficients $\alpha^{(k)}_{bnd}$ and $\alpha^{(k)}_{vol}$ are easily expressed in terms of a projection of the considered forcing onto the optimal forcings:

$$\alpha^{(k)} = \frac{\left(\mathbf{f} \mid \mathbf{f}^{(k)}\right)}{||\mathbf{f}^{(k)}||^2}. \tag{30}$$

With this notation, the projection coefficients for the forcing $\widetilde{\mathbf{f}}_1$ at the cavity end are therefore $\alpha^{(1)}_{bnd} = 1$, and $\alpha^{(k)}_{bnd} = 0$ for $k \geq 1$. By contrast, the projection coefficients $\alpha^{(1)}_{vol}$ and $\alpha^{(2)}_{vol}$ for the forcing arising from higher-harmonic interactions are of the order of 10^{-3}–10^{-2} (figure 15), meaning that $\widetilde{\boldsymbol{\psi}}_{2,-1}$ projects very poorly on the first two optimal volume forcings. In other words, the external forcing $\widetilde{\mathbf{f}}_1$ harnesses *all* the amplification available from the cavity end, while $\widetilde{\boldsymbol{\psi}}_{2,-1}$ only benefits from 0.1–1% of the amplification available in the domain.

One reason for the poor amplification of $\widetilde{\boldsymbol{\psi}}_{2,-1}$ is understood by inspecting its spatial structure in figure 16 and that of $\mathbf{f}^{(1)}_{vol}$ in figure 13. At small and intermediate forcing amplitudes,

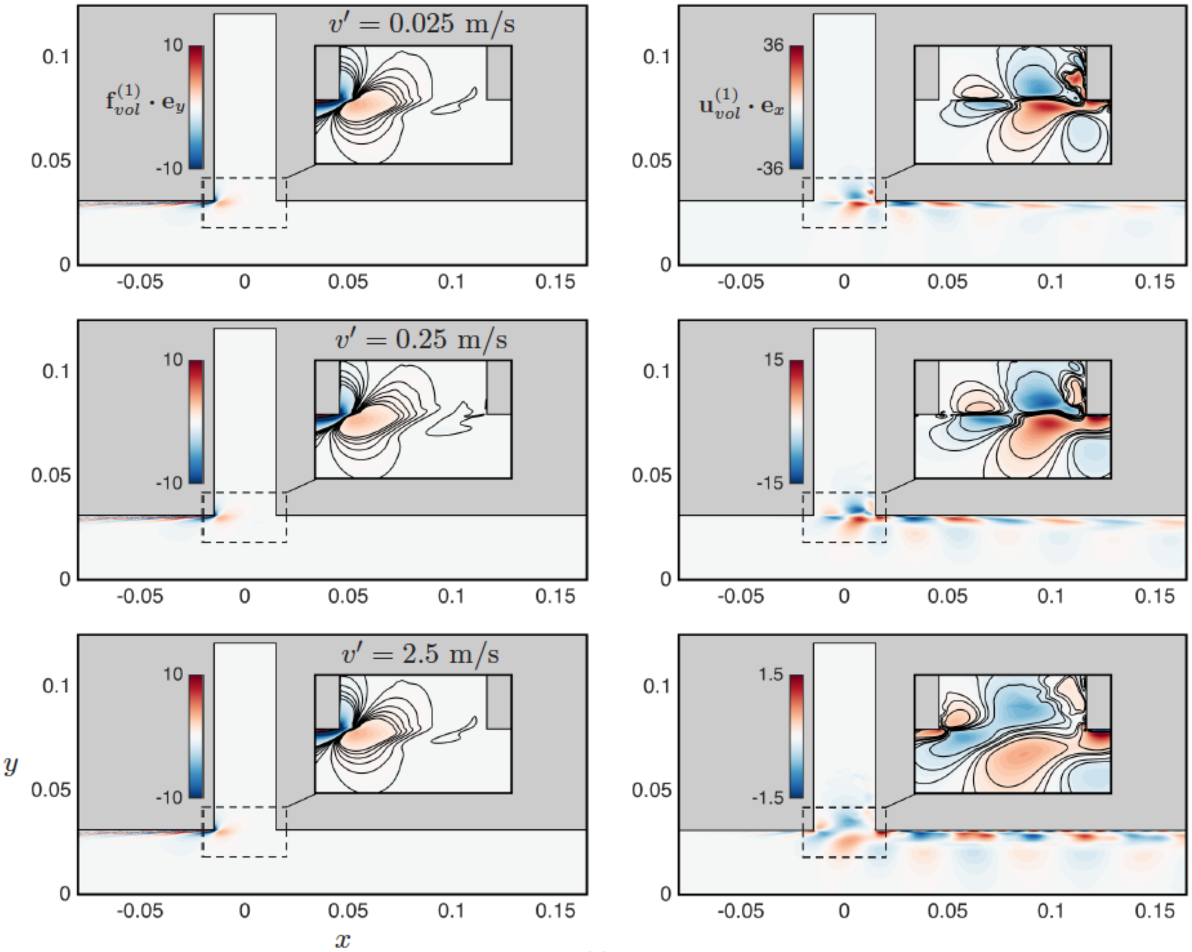

Figure 13: Left: optimal volume forcing $\mathbf{f}_{vol}^{(1)}$ at ω_1 (unit norm; vertical component); Right: corresponding optimal response $\mathbf{u}_{vol}^{(1)}$ (norm $G_{vol}^{(1)}$; streamwise component). Mean flow at forcing amplitudes $v' = 0.025$, 0.25 and 2.5 m/s.

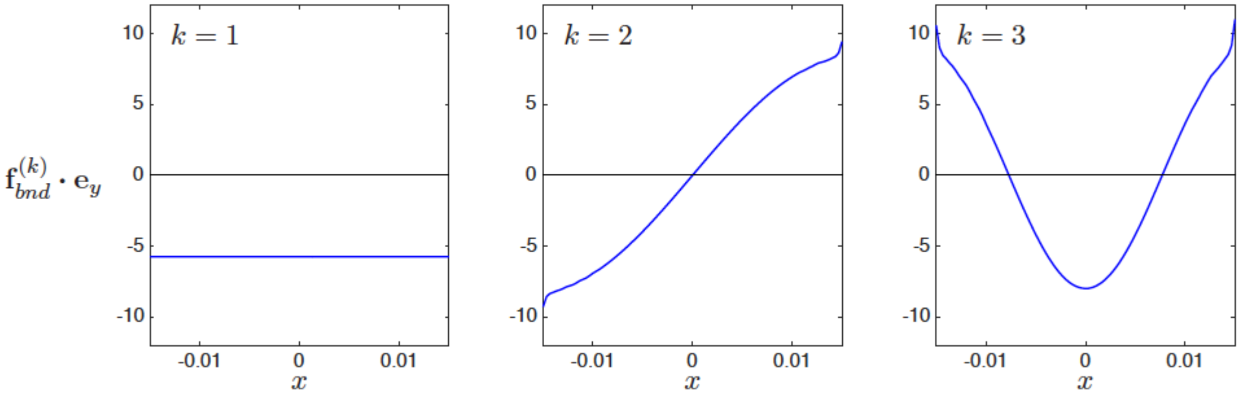

Figure 14: First three optimal boundary forcings at the cavity end Γ_f at ω_1 (real part of vertical component of of unit-norm $\mathbf{f}_{bnd}^{(k)}$). Mean flow forced at amplitude $v' = 0.075$ m/s.

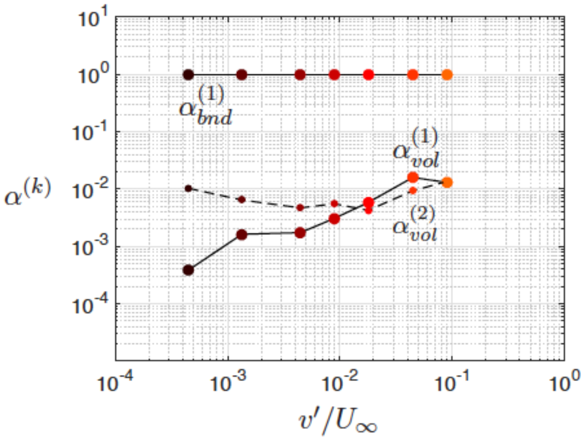

Figure 15: Projection coefficients $\alpha^{(k)}$ on the k-th optimal volume forcing $\mathbf{f}^{(k)}$ at ω_1. Coefficients α_{bnd} and α_{vol} correspond respectively to the external forcing $\widetilde{\mathbf{f}}_1$ applied at the cavity end, and to the volume Reynolds stress forcing $\widetilde{\boldsymbol{\psi}}_{2,-1}$ resulting from higher-harmonic interactions.

Reynolds stresses are concentrated in the downstream region of the cavity, while the optimal forcing is localised around the upstream corner. At larger forcing amplitudes, the spatial overlap is better but the projection is still small because the structures remain essentially orthogonal: for instance, while $\mathbf{f}_{vol}^{(1)} \cdot \mathbf{e}_y$ is uniform over the whole height of the shear layer, $\widetilde{\boldsymbol{\psi}}_{2,-1} \cdot \mathbf{e}_y$ changes sign.

5 Sensitivity analysis

Using the linear response to harmonic forcing around the mean flow, we have gained understanding about amplification and saturation in the turbulent mixing layer over a deep cavity. It is now natural to investigate flow control in order to reduce or increase the acoustic level. Considering the acoustic forcing $\widetilde{\mathbf{f}}_1$ (frequency and spatial shape) as given, one possible strategy is to modify the mean flow $\overline{\mathbf{U}}$ (e.g. using wall actuation or a passive control device), which in turn will modify the linear response $\widetilde{\mathbf{u}}_1$. How much the gain G is affected by a *given* flow modification can be found by recomputing the response. However, a systematic study aiming

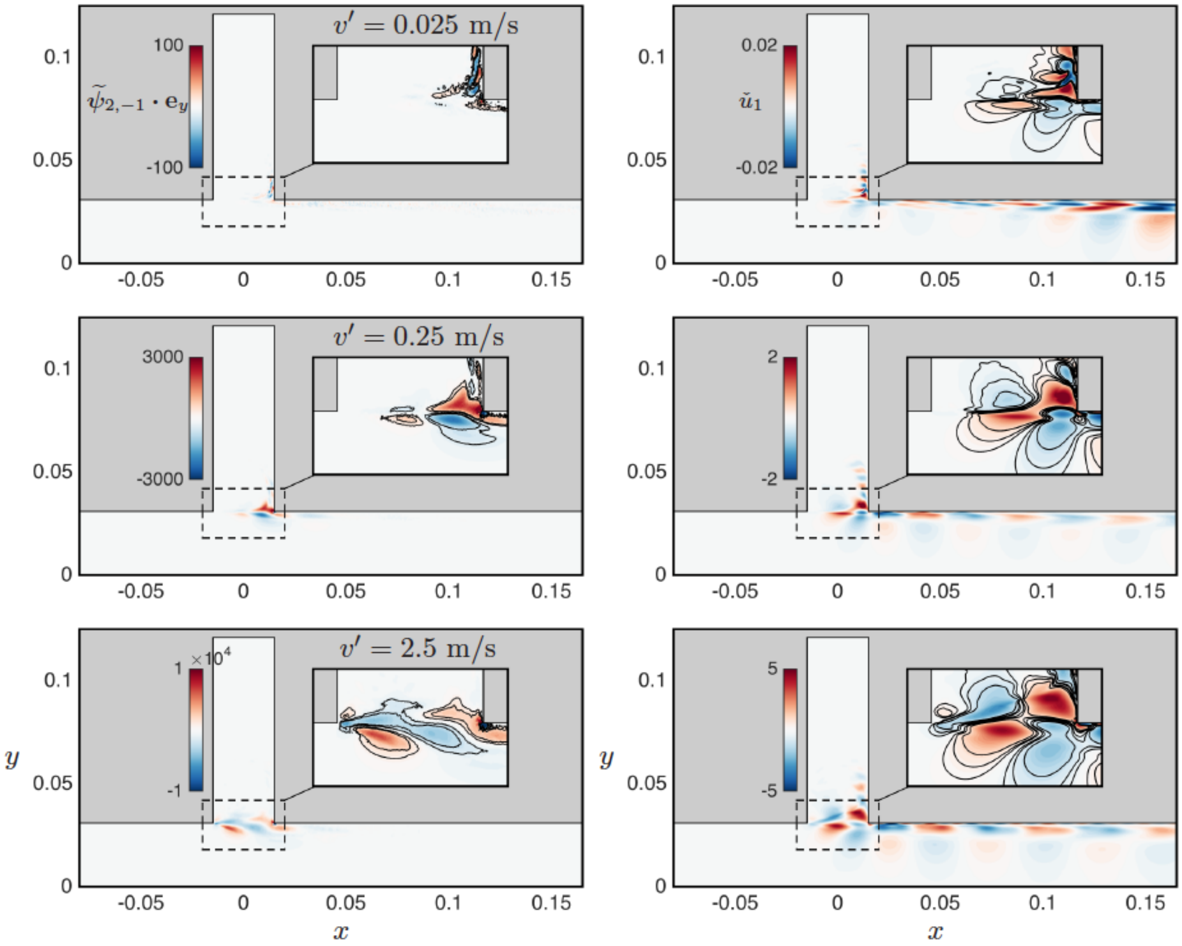

Figure 16: Left: Reynolds stress divergence $\widetilde{\boldsymbol{\psi}}_{2,-1}$ forcing the flow at ω_1, from LES. Right: linear response $\check{\mathbf{u}}_1$ to $\widetilde{\boldsymbol{\psi}}_{2,-1}$, from LNSE. External forcing at ω_1, amplitudes $v' = 0.025$, 0.25 and 2.5 m/s.

at finding the most sensitive regions would imply a large computational cost. A more efficient method consists in predicting the effect of *any* small-amplitude flow modification using adjoint-based sensitivity.

5.1 Adjoint-based sensitivity: background

Sensitivity analysis was introduced in the context of hydrodynamic linear stability by [Hill, 1992], and later used in various parallel ([Bottaro et al., 2003]), non-parallel two-dimensional ([Giannetti and Luchini, 2 Marquet et al., 2008, Meliga et al., 2010]) and three-dimensional flows ([Fani et al., 2012]) and in thermoacoustic systems ([Magri and Juniper, 2013]) to compute the gradient

$$\boldsymbol{\nabla}_{*} \lambda = \frac{\mathrm{d}\lambda}{\mathrm{d}*} \tag{31}$$

of an eigenvalue $\lambda = \sigma + i\omega$ with respect to a variety of modifications $(*)$: (i) steady flow modification, (ii) steady volume/boundary control, (iii) hypothetical localised "velocity-to-force" feedback ("structural sensitivity"). (See [Chomaz, 2005] for more details about structural sensitivity, and [Luchini and Bottaro, 2014] for a broad review about adjoint equations.) The gradient (31) is a useful information since it immediately predicts, via a simple scalar product, the first-order variation $\lambda \to \lambda + \delta\lambda$ induced by any small-amplitude modification: for instance, a flow modification $\mathbf{U} \to \mathbf{U} + \boldsymbol{\delta}\mathbf{U}$ induces an eigenvalue variation

$$\delta\lambda = \left(\boldsymbol{\nabla}_{\mathbf{U}} \lambda \,\middle|\, \boldsymbol{\delta}\mathbf{U} \right) = \left(\frac{\mathrm{d}\lambda}{\mathrm{d}\mathbf{U}} \,\middle|\, \boldsymbol{\delta}\mathbf{U} \right).$$

For linearly stable flows, [Brandt et al., 2011] extended sensitivity analysis to the linear response to harmonic *volume* forcing. They found that the sensitivity of the (squared) harmonic gain G^2 with respect to a modification of the flow $\mathbf{U}$ (case (i) above) is given by

$$\boldsymbol{\nabla}_{\mathbf{U}} G^2_{vol} = 2 G^2_{vol} \mathrm{Re} \left\{ -\boldsymbol{\nabla}\mathbf{u}^H \cdot \mathbf{f}_{vol} + \boldsymbol{\nabla}\mathbf{f}_{vol} \cdot \mathbf{u}^* \right\}, \tag{32}$$

where $\mathbf{u}$ is the response to the volume forcing $\mathbf{f}_{vol}$, and $(\cdot)^H$ denotes Hermitian transpose (conjugate transpose). [Boujo and Gallaire, 2015] considered *boundary* forcing $\mathbf{f}_{bnd}$, in which case the sensitivity of the harmonic gain to flow modification is

$$\boldsymbol{\nabla}_{\mathbf{U}} G^2_{bnd} = 2 \mathrm{Re} \left\{ -\boldsymbol{\nabla}\mathbf{u}^H \cdot \mathbf{u}^\dagger + \boldsymbol{\nabla}\mathbf{u}^\dagger \cdot \mathbf{u}^* \right\}, \tag{33}$$

where $\mathbf{u}$ is the response to the boundary forcing $\mathbf{f}_{bnd}$, and the adjoint perturbation $\mathbf{u}^\dagger$ is a solution of the adjoint resolvent problem with $\mathbf{u}$ as volume forcing (see Appendix B for details). From the knowledge of (32) or (33), one can proceed to compute the sensitivity to control (case (ii) above).

Recently, [Qadri and Schmid, 2017] proposed an equivalent to structural sensitivity (case (iii) above) for the amplification of harmonic *volume* forcing. Rearranging their expression, the overall gain variation for a unit feedback localised in $\mathbf{x} = \mathbf{x}_0$ can be recast as

$$\delta(G^2_{vol}) = -2 G^2_{vol} \mathrm{Re} \left\{ \mathbf{f}_{vol}(\mathbf{x}_0) \cdot \mathbf{u}(\mathbf{x}_0) \right\}. \tag{34}$$

When considering *boundary* forcing, an additional intermediate step is necessary: in this case, the gain variation for a localised unit feedback is

$$\delta(G^2_{bnd}) = -2 \mathrm{Re} \left\{ \mathbf{u}^\dagger(\mathbf{x}_0) \cdot \mathbf{u}(\mathbf{x}_0) \right\}, \tag{35}$$

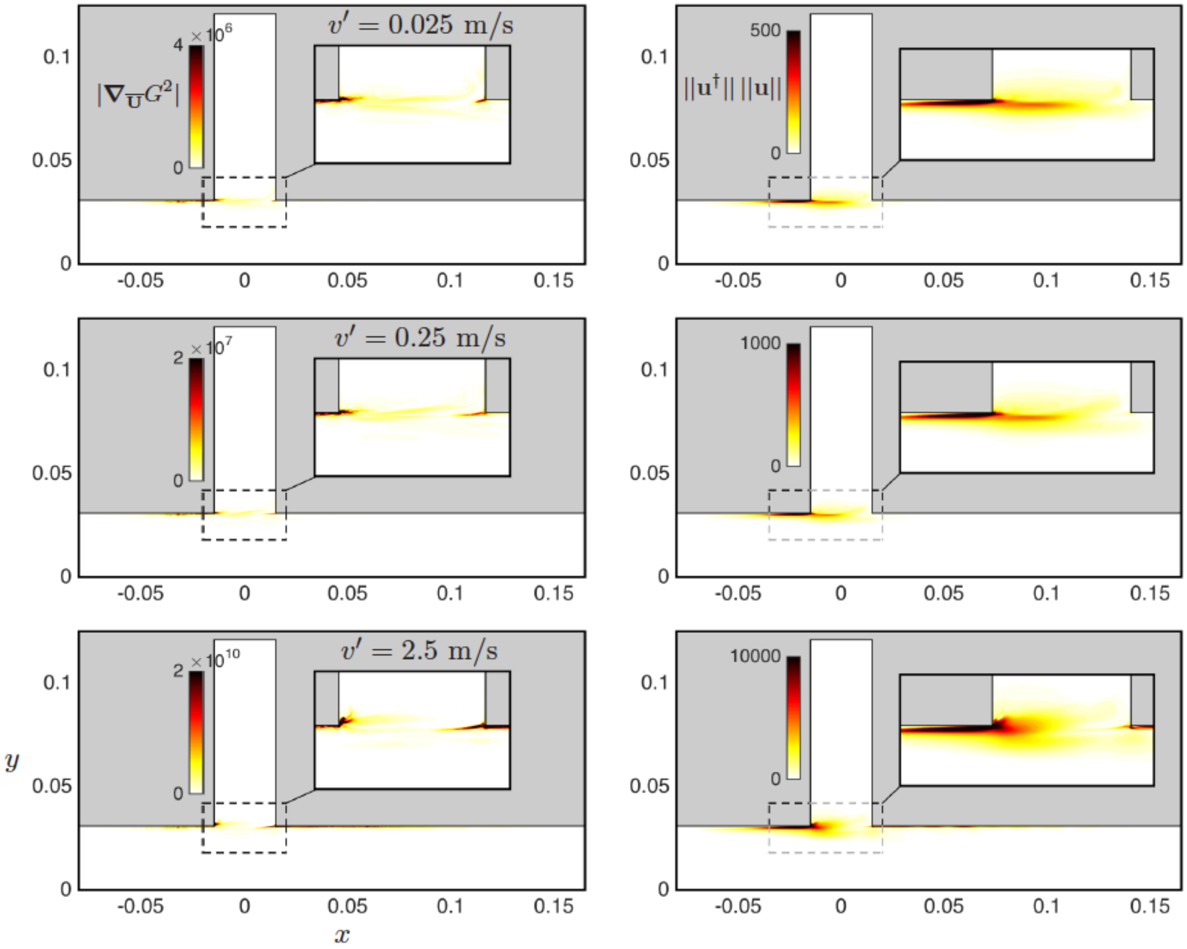

Figure 17: Sensitivity of the linear optimal gain $G^2_{opt}(\omega_1)$, for harmonic forcing at the cavity end Γ_f. (a) Magnitude of the sensitivity with respect to mean flow modification (33). (b) Structural sensitivity (35), i.e. sensitivity with respect to a localised feedback. Forcing amplitudes $v' = 0.025$, 0.25 and 2.5 m/s.

where, again, $\mathbf{u}^\dagger$ is a solution of the adjoint resolvent problem with $\mathbf{u}$ as volume forcing (see details in Appendix B). A simple way to analyse the sensitivity of the harmonic gain with respect to localised feedback is to look at the space-dependent product

$$||\mathbf{f}_{vol}(\mathbf{x}_0)||\,||\mathbf{u}(\mathbf{x}_0)|| \qquad \text{or} \qquad ||\mathbf{u}^\dagger(\mathbf{x}_0)||\,||\mathbf{u}(\mathbf{x}_0)||, \tag{36}$$

which is analogous to the structural sensitivity of an eigenvalue (product of the direct and adjoint modes).

5.2 Sensitivity of the optimal gain

In the following we investigate the sensitivity of the optimal harmonic gain for boundary forcing at the cavity end Γ_f, at frequency ω_1. The sensitivity to mean flow modification (33) and structural sensitivity (35) are shown in figure 17. Both reach their largest magnitude in a localised region near the upstream cavity corner (and, to a lesser extent, in the boundary layer upstream of the cavity as well as in the mixing layer; a second region of large sensitivity appears at the downstream corner as the forcing amplitude v' increases). Therefore, the linear

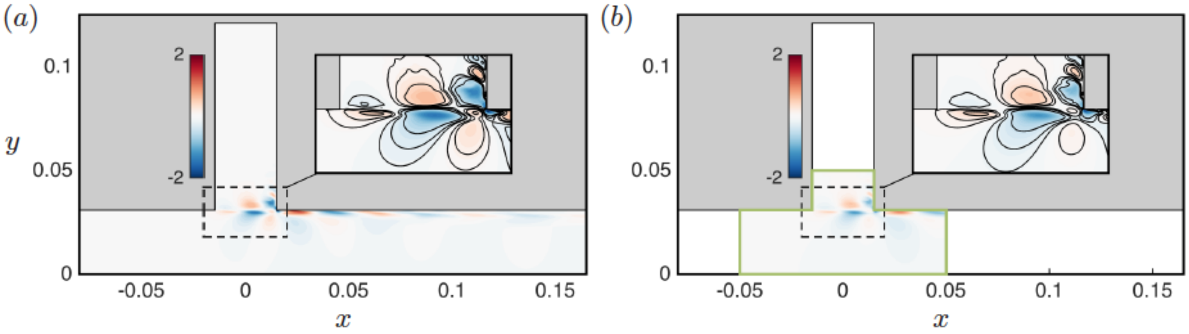

Figure 18: Effect of the size of the LNSE domain used to compute the linear response (frequency ω_1, forcing amplitude $v' = 0.075$ m/s). (*a*) Reference domain I. (*b*) Smaller domain D_3^{xy}.

amplification between optimal boundary forcing and optimal response is the most sensitive to modifications near the upstream corner.

This is consistent with the fact that most of the amplification is driven by the mean shear: acoustic forcing induces perturbations near the upstream corner, which are then amplified in the mixing layer. Any control aiming at modifying the amplification should therefore target the upstream corner. This also explains why saturation is more marked once fluctuations (Reynolds stresses) have moved upstream, in the region where the mean flow is more sensitive to their effect.

We recall from § 4.2 that (i) the responses to optimal boundary and volume forcing are very similar (in terms of spatial structure), and that (ii) the first optimal gain is almost always much larger that the following optimal gains. These two elements point to a robust amplification mechanism in the mixing layer, fairly insensitive to the exact shape and location of the forcing. In addition, we note that the adjoint perturbation $\mathbf{u}^\dagger$ in the sensitivities (33) and (35) looks similar to the optimal response $\mathbf{f}^{(opt)}$, which leads to large sensitivities in the exact same regions for volume forcing (not shown) and boundary forcing (fig. 17).

Finally, we observe that the linear gain does not vary substantially when reducing the size of the computational domain, as long as the boundaries are not too close to the region of large structural sensitivity (see details in Appendix C). The spatial structure of the response is unaffected too (figure 18). This is in agreement with [Giannetti and Luchini, 2007], who found a similar behaviour for the leading eigenvalue and eigenmode of the flow past a circular cylinder at $Re = 50$: they hypothesised that "*the characteristics of the global mode are dictated mainly by the conditions existing in the region where values of*" structural sensitivity "*substantially different from zero are attained*", i.e. where the the global mode and associated adjoint mode overlap. We formulate the same hypothesis in the case of harmonic amplification: the value of the linear gain and the spatial structure of the response are dictated mainly by the flow in the region where structural sensitivity is not small, i.e. where the the response $\mathbf{u}$ and the volume forcing $\mathbf{f}$ (or the adjoint perturbation $\mathbf{u}^\dagger$ associated with boundary forcing) overlap.

6 Conclusion

We consider the turbulent flow over a deep cavity and compute the linear response to a uniform harmonic forcing applied at the cavity end. This forcing mimics a plane acoustic wave corresponding to the dominant acoustic resonance mode (quarter-wave mode) at frequency

ω_1. Calculations are carried out in the framework of the incompressible Linearised Navier–Stokes Equations (LNSE) with an eddy-viscosity turbulence model, and using as linearisation point the mean flow obtained from nonlinear Large-Eddy Simulations (LES) with a similar harmonic forcing at several amplitudes spanning more than two orders of magnitude. The influence of higher harmonics on the mean flow is automatically accounted for via LES, while their influence on coherent oscillations at ω_1 is neglected. The aim of the work is to assess the ability of this LNSE-based procedure to yield accurate results in terms of spatial structure and response amplitude, and to capture the saturation mechanism that, ultimately, would set the limit-cycle oscillation amplitude in a self-excited aeroacoustic resonance.

We find that the response amplitude is well predicted, both with a hydrodynamic measure (kinetic energy) and with an acoustic measure (Coriolis force involved in acoustic power generation). Vortical structures in the shear layer are in good agreement too, except at very large forcing amplitudes. The gain (amplification of the forcing) is largest in the unforced case and decreases with forcing amplitude. This is consistent with the following saturation scenario: as the amplitude of oscillations grows, their nonlinear interaction (in the form of Reynolds stresses) modifies the mean flow, and shear-driven amplification in the thickened shear layer is reduced. We observe that this good agreement is possible even though higher harmonics, neglected in the LNSE, are not small. This suggests that the mean flow contains all important nonlinearities.

We also note with a resolvent analysis that the optimal boundary forcing (t.e. the forcing which undergoes the largest possible amplification) at the cavity end is uniform, i.e. the forcing we prescribe in our study has precisely the optimal shape and benefits from the entire potential for amplification available at the cavity end. By contrast, the nonlinear interaction of the first and second harmonics which forces the flow at ω_1 is projected poorly on the optimal volume forcing and does not take advantage efficiently of the potential for amplification available in the domain.

Finally, sensitivity analysis identifies the upstream boundary layer and upstream cavity corner as regions where both localised feedback and mean flow modification have the largest effect on harmonic amplification, an information that can contribute to a systematic and computationally inexpensive control design.

A future goal is to extend the method to the prediction of limit-cycle amplitudes in self-excited aeroacoustic resonances. This should be accomplished in a stand-alone fashion, i.e. without relying on expensive nonlinear simulations such as LES to compute the mean flow. Extending semi-linear self-consistent models ([Mantič-Lugo et al., 2014, Mantič-Lugo and Gallaire, 2016]) to turbulent flows would, if technically possible, constitute a promising method.

Appendix A. Convergence study on mesh size

The influence of the mesh size on the LNSE results is analysed with a convergence study involving four meshes, M_1 to M_4. All meshes share the same structure: coarser at the inlet and outlet, and gradually finer toward the shear layer. Mesh M_1 contains $N_{SL} = 315$ vertices across the shear layer $\{-W/2 \leq x \leq W/2, y = D/2\}$, resulting in approximately N_e=120 000 triangular elements in the whole domain I. Meshes M_2 to M_4 are obtained by applying to M_1 a uniform refinement of factor 1.33, 1.67 and 2, resulting in approximately N_e=204 000, 331 000 and 458 000 elements, respectively (table 1).

Convergence is reported in figure 19 for two selected quantities: harmonic gain G_{bnd} for boundary forcing $\widetilde{\mathbf{f}}_1$ on Γ_f, and first optimal gain $G_{vol}^{(1)}$ for volume forcing in I (both at frequency ω_1, around the LES mean flow at $v' = 0.075$ m/s). While G_{bnd} is already well converged on

	M_1	M_2	$\mathbf{M}_3$	M_4
N_{SL}	315	420	**525**	630
N_v	60 743	103 045	**166 464**	230 240
N_e	120 214	204 388	**330 794**	457 921

Table 1: Meshes used for the convergence study: number of vertices across the shear layer, total number of vertices and total number of triangular elements.

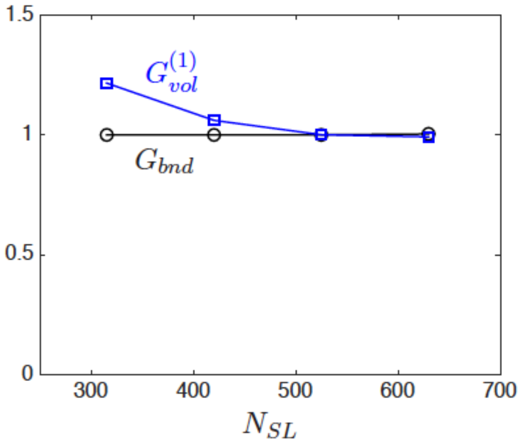

Figure 19: Influence of mesh size: convergence with N_{SL}, the number of vertices across the shear layer (i.e. along the line $\{-W/2 \leq x \leq W/2, y = D/2\}$). Circles: harmonic gain for boundary forcing on Γ_f; squares: first optimal gain for volume forcing in I. Gains are normalised by their values obtained on the reference mesh M_3 (N_{SL}=525, see table 1). Forcing frequency ω_1, amplitude $v' = 0.075$ m/s.

the relatively coarser mesh M_1 (0.3% variation between M_1 and M_4), $G_{vol}^{(1)}$ requires the finer mesh M3 for a satisfactory convergence (0.9% variation between M_3 and M_4). As mentioned in § 3.2, mesh M_3 is therefore used throughout the paper.

Appendix B. Sensitivity of harmonic gain

Recall the LNSE (15) or, equivalently, the definition of the resolvent operator (27):

$$(i\omega + \mathbf{L})\mathbf{u} = \mathbf{f} \quad \Leftrightarrow \quad \mathbf{u} = (i\omega + \mathbf{L})^{-1}\mathbf{f} = \mathbf{R}(\omega)\mathbf{f}. \tag{37}$$

For the sake of simplicity and generality, we drop tildes $\tilde{\cdot}$ and omit the dependence on the mean flow $\overline{\mathbf{U}}$. We distinguish two cases: harmonic forcing $\mathbf{f}_{vol}$ applied in the volume,

$$(i\omega + \mathbf{L})\mathbf{u}_{vol} = \mathbf{f}_{vol} \quad \text{in I}, \qquad \mathbf{u}_{vol} = \mathbf{0} \quad \text{on } \Gamma_f, \tag{38}$$

and harmonic forcing $\mathbf{f}_{bnd}$ applied at a boundary,

$$(i\omega + \mathbf{L})\mathbf{u}_{bnd} = \mathbf{0} \quad \text{in I}, \qquad \mathbf{u}_{bnd} = \mathbf{f}_{bnd} \quad \text{on } \Gamma_f. \tag{39}$$

We write in short those two problems as

$$\mathbf{u}_{vol} = \mathbf{R}_{vol}\mathbf{f}_{vol} \qquad \text{and} \qquad \mathbf{u}_{bnd} = \mathbf{R}_{bnd}\mathbf{f}_{bnd}. \tag{40}$$

For a given forcing $\mathbf{f}$, a variation of the NS operator $\mathbf{L} \rightarrow \mathbf{L} + \boldsymbol{\delta}\mathbf{L}$ induces a variation of the response $\mathbf{u} \rightarrow \mathbf{u} + \boldsymbol{\delta}\mathbf{u}$. Substituting into (38)-(39), expanding and keeping only zeroth- and first-order terms yields for volume forcing:

$$(i\omega + \mathbf{L})\mathbf{u}_{vol} + (i\omega + \mathbf{L})\boldsymbol{\delta}\mathbf{u}_{vol} + \boldsymbol{\delta}\mathbf{L}\,\mathbf{u}_{vol} = \mathbf{f}_{vol} \quad \text{in I}, \qquad \mathbf{u}_{vol} + \boldsymbol{\delta}\mathbf{u}_{vol} = \mathbf{0} \quad \text{on } \Gamma_f, \tag{41}$$

and for boundary forcing:

$$(i\omega + \mathbf{L})\mathbf{u}_{bnd} + (i\omega + \mathbf{L})\boldsymbol{\delta}\mathbf{u}_{bnd} + \boldsymbol{\delta}\mathbf{L}\,\mathbf{u}_{bnd} = \mathbf{0} \quad \text{in I}, \qquad \mathbf{u}_{bnd} + \boldsymbol{\delta}\mathbf{u}_{bnd} = \mathbf{f}_{bnd} \quad \text{on } \Gamma_f. \tag{42}$$

Upon subtracting (38) and (39), respectively, both problems reduce to:

$$(i\omega + \mathbf{L})\boldsymbol{\delta}\mathbf{u} = -\boldsymbol{\delta}\mathbf{L}\,\mathbf{u} \quad \text{in I}, \qquad \boldsymbol{\delta}\mathbf{u} = \mathbf{0} \quad \text{on } \Gamma_f. \tag{43}$$

That is, in both cases (volume forcing and boundary forcing), the response variation $\boldsymbol{\delta}\mathbf{u}$ is solution of a *volume resolvent* problem (volume forcing $-\boldsymbol{\delta}\mathbf{L}\,\mathbf{u}$ and homogeneous boundary conditions):

$$\boldsymbol{\delta}\mathbf{u}_{vol} = -\mathbf{R}_{vol}\boldsymbol{\delta}\mathbf{L}_{vol}\mathbf{u}_{vol} \qquad \text{and} \qquad \boldsymbol{\delta}\mathbf{u}_{bnd} = -\mathbf{R}_{vol}\boldsymbol{\delta}\mathbf{L}_{bnd}\mathbf{u}_{bnd} \tag{44}$$

We now proceed to find the gain variation induced by the variation of the NS operator. The variation of the gain

$$G^2 = \frac{||\mathbf{u}||^2}{||\mathbf{f}||^2} = \frac{(\,\mathbf{u}\,|\,\mathbf{u}\,)}{(\,\mathbf{f}\,|\,\mathbf{f}\,)}, \tag{45}$$

reads at zeroth and first orders:

$$G^2 + \delta(G^2) = \frac{(\,\mathbf{u} + \boldsymbol{\delta}\mathbf{u}\,|\,\mathbf{u} + \boldsymbol{\delta}\mathbf{u}\,)}{(\,\mathbf{f}\,|\,\mathbf{f}\,)} = \frac{(\,\mathbf{u}\,|\,\mathbf{u}\,)}{(\,\mathbf{f}\,|\,\mathbf{f}\,)} + 2\mathrm{Re}\left\{\frac{(\,\mathbf{u}\,|\,\boldsymbol{\delta}\mathbf{u}\,)}{(\,\mathbf{f}\,|\,\mathbf{f}\,)}\right\}, \tag{46}$$

i.e. after subtracting (45) and multiplying by $||\mathbf{f}||^2$:

$$\delta(G^2)||\mathbf{f}||^2 = 2\mathrm{Re}\left\{(\,\mathbf{u}\,|\,\boldsymbol{\delta}\mathbf{u}\,)\right\}. \tag{47}$$

Substituting the response variation $\boldsymbol{\delta}\mathbf{u}$ from (44), and using the definition of an adjoint operator, one obtains for volume forcing:

$$\begin{aligned}
\delta(G_{vol}^2)||\mathbf{f}_{vol}||^2 &= 2\mathrm{Re}\left\{(\,\mathbf{u}_{vol}\,|\,-\mathbf{R}_{vol}\boldsymbol{\delta}\mathbf{L}_{vol}\mathbf{u}_{vol}\,)\right\} \\
&= -2\mathrm{Re}\left\{\left(\mathbf{R}_{vol}^{\dagger}\mathbf{u}_{vol}\,\middle|\,\boldsymbol{\delta}\mathbf{L}_{vol}\mathbf{u}_{vol}\right)\right\} \\
&= -2\mathrm{Re}\left\{\left(G_{vol}^2\mathbf{f}_{vol}\,\middle|\,\boldsymbol{\delta}\mathbf{L}_{vol}\mathbf{u}_{vol}\right)\right\},
\end{aligned} \tag{48}$$

and for inlet forcing:

$$\begin{aligned}
\delta(G_{bnd}^2)||\mathbf{f}_{bnd}||^2 &= 2\mathrm{Re}\left\{(\,\mathbf{u}_{bnd}\,|\,-\mathbf{R}_{vol}\boldsymbol{\delta}\mathbf{L}_{bnd}\mathbf{u}_{bnd}\,)\right\} \\
&= -2\mathrm{Re}\left\{\left(\mathbf{R}_{vol}^{\dagger}\mathbf{u}_{bnd}\,\middle|\,\boldsymbol{\delta}\mathbf{L}_{bnd}\mathbf{u}_{bnd}\right)\right\} \\
&= -2\mathrm{Re}\left\{\left(\mathbf{u}^{\dagger}\,\middle|\,\boldsymbol{\delta}\mathbf{L}_{bnd}\mathbf{u}_{bnd}\right)\right\}.
\end{aligned} \tag{49}$$

In (48) we have used the relation $\mathbf{R}_{vol}^{\dagger}\mathbf{u}_{vol} = G_{vol}^2\mathbf{f}_{vol}$ ([Brandt et al., 2011, Boujo and Gallaire, 2015]). In (49), however, we have introduced $\mathbf{u}^{\dagger} = \mathbf{R}_{vol}^{\dagger}\mathbf{u}_{bnd}$ (defined in the domain), which is *not*

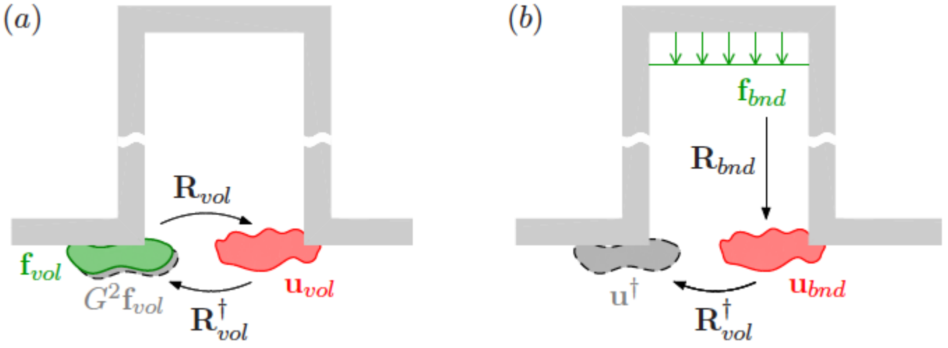

Figure 20: (*a*) Harmonic *volume* forcing $\mathbf{f}_{vol}$ and associated response $\mathbf{u}_{vol}$, from which one can compute the gain sensitivities (32) and (34). (*b*) Harmonic *boundary* forcing $\mathbf{f}_{bnd}$ and associated response $\mathbf{u}_{bnd}$. The adjoint $\mathbf{u}^{\dagger}$ is needed to compute the gain sensitivities (33) and (35).

equal to $G_{bnd}^2\mathbf{f}_{bnd}$ (defined on the boundary). Note that one can choose a unit forcing, $||\mathbf{f}|| = 1$, since the gain is linear.

As illustrated in figure 20, knowing $\mathbf{f}_{vol}$ and $\mathbf{u}_{vol}$ is sufficient to compute the gain sensitivity in the case of *volume* forcing; the adjoint $\mathbf{u}^{\dagger}$ is necessary, however, to compute the gain sensitivity in the case of *boundary* forcing.

Expressions (48)-(49) allow one to easily compute gain variations $\delta(G^2)$ for any small-amplitude modification $\boldsymbol{\delta}\mathbf{L}$ of the NS operator, without solving explicitly for the modified response $\mathbf{u} + \boldsymbol{\delta}\mathbf{u}$. These expressions are general, but we can now make them more specific for two particular modifications $\boldsymbol{\delta}\mathbf{L}$ of interest.

First, when the mean flow is modified, $\overline{\mathbf{U}} \rightarrow \overline{\mathbf{U}} + \boldsymbol{\delta}\overline{\mathbf{U}}$, the NS operator variation reads

$$\boldsymbol{\delta}\mathbf{L}\,\mathbf{u} = (\mathbf{u}\cdot\boldsymbol{\nabla})\boldsymbol{\delta}\overline{\mathbf{U}} + (\boldsymbol{\delta}\overline{\mathbf{U}}\cdot\boldsymbol{\nabla})\mathbf{u}, \tag{50}$$

and one obtains after a few manipulations:

$$\begin{aligned} \delta(G_{vol}^2) &= -2G_{vol}^2\mathrm{Re}\left\{\left(\mathbf{f}_{vol}\,\middle|\,(\mathbf{u}_{vol}\cdot\boldsymbol{\nabla})\boldsymbol{\delta}\overline{\mathbf{U}} + (\boldsymbol{\delta}\overline{\mathbf{U}}\cdot\boldsymbol{\nabla})\mathbf{u}_{vol}\right)\right\}, \\ &= -2G_{vol}^2\mathrm{Re}\left\{\left(\boldsymbol{\nabla}\mathbf{u}_{vol}^H\cdot\mathbf{f}_{vol} - \boldsymbol{\nabla}\mathbf{f}_{vol}\cdot\mathbf{u}_{vol}^*\,\middle|\,\boldsymbol{\delta}\overline{\mathbf{U}}\right)\right\}, \end{aligned} \tag{51}$$

$$\begin{aligned} \delta(G_{bnd}^2) &= -2\mathrm{Re}\left\{\left(\mathbf{u}^{\dagger}\,\middle|\,(\mathbf{u}_{bnd}\cdot\boldsymbol{\nabla})\boldsymbol{\delta}\overline{\mathbf{U}} + (\boldsymbol{\delta}\overline{\mathbf{U}}\cdot\boldsymbol{\nabla})\mathbf{u}_{bnd}\right)\right\} \\ &= -2\mathrm{Re}\left\{\left(\boldsymbol{\nabla}\mathbf{u}_{bnd}^H\cdot\mathbf{u}^{\dagger} - \boldsymbol{\nabla}\mathbf{u}^{\dagger}\cdot\mathbf{u}_{bnd}^*\,\middle|\,\boldsymbol{\delta}\overline{\mathbf{U}}\right)\right\}, \end{aligned} \tag{52}$$

hence the expressions (32)-(33) of the gain sensitivity $\boldsymbol{\nabla}_{\overline{\mathbf{U}}}G^2$.

Second, for a feedback localised in $\mathbf{x} = \mathbf{x}_0$ in the form of a "velocity-to-force" coupling, the NS operator variation reads

$$\boldsymbol{\delta}\mathbf{L}\,\mathbf{u} = \mathbf{C}(\mathbf{x})\mathbf{u} = \delta(\mathbf{x}-\mathbf{x}_0)\mathbf{C}_0\mathbf{u} \tag{53}$$

where $\delta(\mathbf{x})$ is the 2D delta Dirac function. Expressions (48)-(49) therefore become

$$\begin{aligned} \delta(G_{vol}^2) &= -2G_{vol}^2\mathrm{Re}\left\{\left(\mathbf{f}_{vol}\,\middle|\,\delta(\mathbf{x}-\mathbf{x}_0)\mathbf{C}_0\mathbf{u}_{vol}\right)\right\} \\ &= -2G_{vol}^2\mathrm{Re}\left\{\mathbf{f}_{vol}(\mathbf{x}_0)\cdot\mathbf{C}_0\mathbf{u}_{vol}(\mathbf{x}_0)\right\}, \end{aligned} \tag{54}$$

$$\begin{aligned} \delta(G_{bnd}^2) &= -2\mathrm{Re}\left\{\left(\mathbf{u}^{\dagger}\,\middle|\,\delta(\mathbf{x}-\mathbf{x}_0)\mathbf{C}_0\mathbf{u}_{bnd}\right)\right\} \\ &= -2\mathrm{Re}\left\{\mathbf{u}^{\dagger}(\mathbf{x}_0)\cdot\mathbf{C}_0\mathbf{u}_{bnd}(\mathbf{x}_0)\right\}. \end{aligned} \tag{55}$$

	REF (I)	D_1^x	D_2^x	D_3^x	D_1^y	D_2^y	D_3^y	D_4^y	D_1^{xy}	D_2^{xy}	D_3^{xy}
x_1	**-80**	-40	-30	-20	-	-	-	-	-50	-50	-50
x_2	**165**	40	30	20	-	-	-	-	50	50	50
y_2	**121**	-	-	-	80	50	40	40	80	50	50
y_1	**-31**	-	-	-	-	0	10	20	-	-	0

Table 2: Domains used for convergence study, with various locations of the inlet (x_1), outlet (x_2), cavity end (y_2) and lower channel wall (y_1). Dimensions in mm. Only values different from the reference domain Iare indicated. See also figure 21.

Choosing the identity matrix for $\mathbf{C}_0$ (i.e. a velocity sensed in the x (resp. y) direction results in a force in the x (resp. y) direction only), one recovers the expressions (34)-(35) of the gain sensitivity $\boldsymbol{\nabla}_{\mathbf{fb}} G^2$.

Appendix C. Influence of domain size

A series of smaller LNSE domains are used to investigate which flow regions are important to capture the linear response to harmonic forcing. Only the LNSE domain is modified: all linear response calculations are performed with the same LES mean flow. The positions of the boundaries are varied as follows (see table 2): inlet (x_1) and outlet (x_2) in domains D^x, cavity end (y_2) and lower channel wall (y_1) in domains D^y, and all four boundaries in domains D^{xy}. Note that the uniform harmonic forcing $\mathbf{f}$ is applied on Γ_f, whose position y_2 varies in domains D^y and D^{xy}.

The response measured in terms of kinetic energy (20) and vertical component of the Coriolis force (21) is shown in figure 21, (normalised by values obtained on the largest reference domain I). Note that domains D^y and D^{xy} have a smaller vertical extension than region J, where the response is normally computed.

References

[Alvarez et al., 2004] Alvarez, J., Kerschen, E., and Tumin, A. (2004). A theoretical model for cavity acoustic resonances in subsonic flow. In 10th AIAA/CEAS Aeroacoustics Conference. American Institute of Aeronautics and Astronautics.

[Barkley, 2006] Barkley, D. (2006). Linear analysis of the cylinder wake mean flow. Europhysics Letters, 75(5):750–756.

[Bauerheim et al., 2017] Bauerheim, M., Boujo, E., and Noiray, N. (2017). Numerical analysis of the linear and nonlinear vortex-noise coupling mechanisms in a T-junction. In preparation.

[Beneddine et al., 2016] Beneddine, S., Sipp, D., Arnault, A., Dandois, J., and Lesshafft, L. (2016). Conditions for validity of mean flow stability analysis. Journal of Fluid Mechanics, 798:485–504.

[Bottaro et al., 2003] Bottaro, A., Corbett, P., and Luchini, P. (2003). The effect of base flow variation on flow stability. Journal of Fluid Mechanics, 476:293–302.

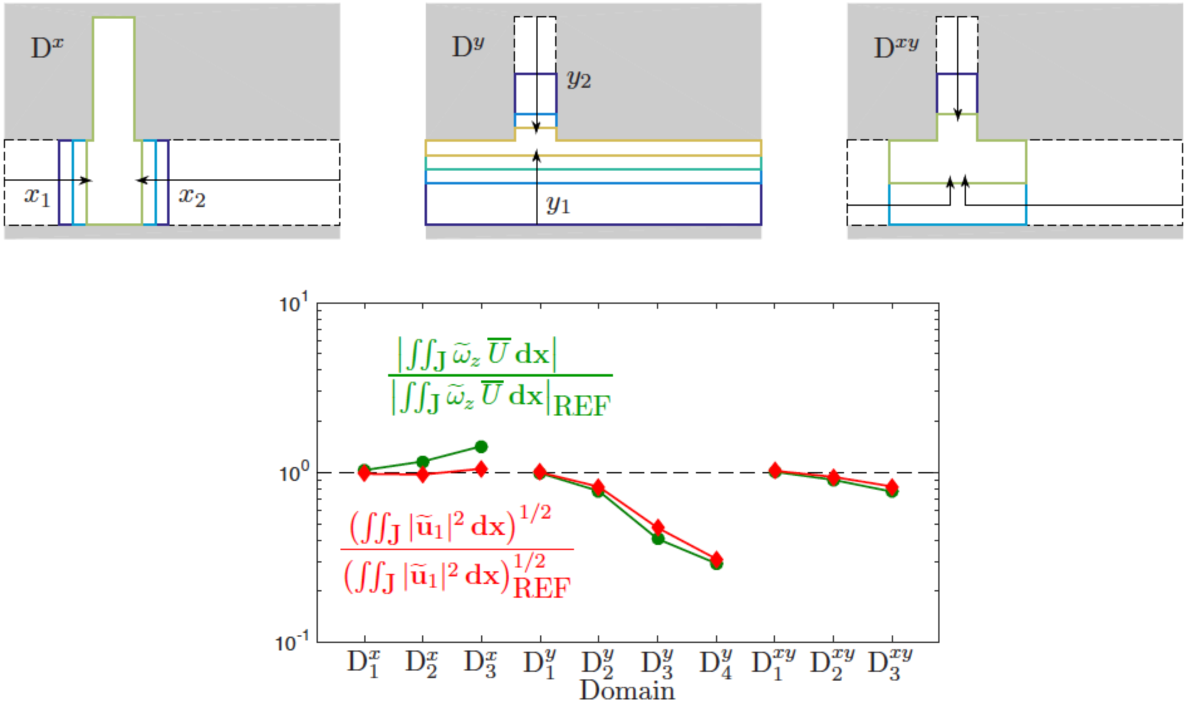

Figure 21: Influence of domain size. Linear harmonic response to boundary forcing on Γ_f. Circles: kinetic energy (20); diamonds: vertical component of the Coriolis force (21). Linear response values are normalised by the values obtained on the largest reference domain I(see table 2). Forcing frequency ω_1, amplitude $v' = 0.075$ m/s.

[Boujo et al., 2013] Boujo, E., Ehrenstein, U., and Gallaire, F. (2013). Open-loop control of noise amplification in a separated boundary layer flow. Physics of Fluids, 25(12).

[Boujo and Gallaire, 2015] Boujo, E. and Gallaire, F. (2015). Sensitivity and open-loop control of stochastic response in a noise amplifier flow: the backward-facing step. Journal of Fluid Mechanics, 762:361392.

[Brandt et al., 2011] Brandt, L., Sipp, D., Pralits, J., and Marquet, O. (2011). Effect of base-flow variation in noise amplifiers: the flat-plate boundary layer. Journal of Fluid Mechanics, 687:503–528.

[Cain et al., 1996] Cain, A., Bower, W., McCotter, F., and Romer, W. (1996). Modeling and prediction of weapons bay acoustic amplitude and frequency. Technical report, VEDA Inc.

[Chomaz, 2005] Chomaz, J. (2005). Global instabilities in spatially developing flows: Non-normality and nonlinearity. Annual Review of Fluid Mechanics, 37:357–392.

[del Álamo and Jiménez, 2006] del Álamo, J. C. and Jiménez, J. (2006). Linear energy amplification in turbulent channels. Journal of Fluid Mechanics, 559:205–213.

[Dergham et al., 2013] Dergham, G., Sipp, D., and Robinet, J.-C. (2013). Stochastic dynamics and model reduction of amplifier flows: the backward facing step flow. Journal of Fluid Mechanics, 719:406–430.

[Edstrand et al., 2016] Edstrand, A. M., Davis, T. B., Schmid, P. J., Taira, K., and Cattafesta, L. N. (2016). On the mechanism of trailing vortex wandering. Journal of Fluid Mechanics, 801.

[Fani et al., 2012] Fani, A., Camarri, S., and Salvetti, M. (2012). Stability analysis and control of the flow in a symmetric channel with a sudden expansion. Physics of Fluids (1994-present), 24(8).

[Farrell and Ioannou, 1993] Farrell, B. F. and Ioannou, P. J. (1993). Stochastic forcing of the linearized Navier–Stokes equations. Physics of Fluids A: Fluid Dynamics, 5(11):2600–2609.

[Garnaud et al., 2013] Garnaud, X., Lesshafft, L., Schmid, P. J., and Huerre, P. (2013). The preferred mode of incompressible jets: linear frequency response analysis. Journal of Fluid Mechanics, 716:189–202.

[Giannetti and Luchini, 2007] Giannetti, F. and Luchini, P. (2007). Structural sensitivity of the first instability of the cylinder wake. Journal of Fluid Mechanics, 581:167–197.

[Gikadi et al., 2014] Gikadi, J., Föller, S., and Sattelmayer, T. (2014). Impact of turbulence on the prediction of linear aeroacoustic interactions: Acoustic response of a turbulent shear layer. Journal of Sound and Vibration, 333:6548–6559.

[Graf and Ziada, 2010] Graf, H. R. and Ziada, S. (2010). Excitation source of a side-branch shear layer. Journal of Sound and Vibration, 329:28252842.

[Hecht, 2012] Hecht, F. (2012). New development in FreeFem++. Journal of Numerical Mathematics, 20(3-4):251–265.

[Hill, 1992] Hill, D. C. (1992). A theoretical approach for analyzing the restabilization of wakes. AIAA 92-0067.

[Howe, 1980] Howe, M. (1980). The dissipation of sound at an edge. Journal of Sound and Vibration, 70(3):407–411.

[Hwang and Cossu, 2010] Hwang, Y. and Cossu, C. (2010). Amplification of coherent streaks in the turbulent Couette flow: an inputoutput analysis at low Reynolds number. Journal of Fluid Mechanics, 643:333–348.

[Iungo et al., 2013] Iungo, G. V., Viola, F., Camarri, S., Porté-Agel, F., and Gallaire, F. (2013). Linear stability analysis of wind turbine wakes performed on wind tunnel measurements. Journal of Fluid Mechanics, 737:499–526.

[Kitsios et al., 2010] Kitsios, V., Cordier, L., Bonnet, J.-P., Ooi, A., and Soria, J. (2010). Development of a nonlinear eddy-viscosity closure for the triple-decomposition stability analysis of a turbulent channel. Journal of Fluid Mechanics, 664:74–107.

[Kooijman et al., 2004] Kooijman, G., Golliard, J., and Hirschberg, A. (2004). Orifice impedance under grazing flow measured with a single microphone method. In 10th AIAA/CEAS Aeroacoustics Conference. American Institute of Aeronautics and Astronautics.

[Luchini and Bottaro, 2014] Luchini, P. and Bottaro, A. (2014). Adjoint equations in stability analysis. Annual Review of Fluid Mechanics, 46(1):493–517.

[Magri and Juniper, 2013] Magri, L. and Juniper, M. P. (2013). Sensitivity analysis of a time-delayed thermo-acoustic system via an adjoint-based approach. Journal of Fluid Mechanics, 719:183–202.

[Mantič-Lugo et al., 2014] Mantič-Lugo, V., Arratia, C., and Gallaire, F. (2014). Self-consistent mean flow description of the nonlinear saturation of the vortex shedding in the cylinder wake. Phys. Rev. Lett., 113:084501.

[Mantič-Lugo and Gallaire, 2016] Mantič-Lugo, V. and Gallaire, F. (2016). Self-consistent model for the saturation mechanism of the response to harmonic forcing in the backward-facing step flow. Journal of Fluid Mechanics, 793:777–797.

[Marquet et al., 2008] Marquet, O., Sipp, D., and Jacquin, L. (2008). Sensitivity analysis and passive control of cylinder flow. Journal of Fluid Mechanics, 615:221–252.

[Marquillie et al., 2011] Marquillie, M., Ehrenstein, U., and Laval, J.-P. (2011). Instability of streaks in wall turbulence with adverse pressure gradient. Journal of Fluid Mechanics, 681:205–240.

[McKeon et al., 2013] McKeon, B. J., Sharma, A. S., and Jacobi, I. (2013). Experimental manipulation of wall turbulence: A systems approach. Physics of Fluids, 25(3):031301.

[Meliga, 2017] Meliga, P. (2017). Harmonics generation and the mechanics of saturation in flow over an open cavity: a second-order self-consistent description. Journal of Fluid Mechanics, 826:503–521.

[Meliga et al., 2012] Meliga, P., Pujals, G., and Serre, E. (2012). Sensitivity of 2-D turbulent flow past a D-shaped cylinder using global stability. Physics of Fluids (1994-present), 24(6).

[Meliga et al., 2010] Meliga, P., Sipp, D., and Chomaz, J.-M. (2010). Open-loop control of compressible afterbody flows using adjoint methods. Physics of Fluids, 22(5):054109.

[Mettot et al., 2014] Mettot, C., Sipp, D., and Bézard, H. (2014). Quasi-laminar stability and sensitivity analyses for turbulent flows: Prediction of low-frequency unsteadiness and passive control. Physics of Fluids (1994-present), 26(4):–.

[Morris, 2011] Morris, S. C. (2011). Shear-layer instabilities: Particle image velocimetry measurements and implications for acoustics. Annual Review of Fluid Mechanics, 43(1):529–550.

[Nakiboğlu et al., 2012] Nakiboğlu, G., Manders, H., and Hirschberg, A. (2012). Aeroacoustic power generated by a compact axysymmetric cavity: prediction of self-sustained oscillation and influence of the depth. Journal of Fluid Mechanics, 703:163–191.

[Oberleithner et al., 2014] Oberleithner, K., Paschereit, C. O., and Wygnanski, I. (2014). On the impact of swirl on the growth of coherent structures. Journal of Fluid Mechanics, 741:156–199.

[Oberleithner et al., 2015] Oberleithner, K., Schimek, S., and Paschereit, C. O. (2015). Shear flow instabilities in swirl-stabilized combustors and their impact on the amplitude dependent flame response: A linear stability analysis. Combustion and Flame, 162(1):86–99.

[Piot et al., 2006] Piot, E., Casalis, G., Muller, F., and Bailly, C. (2006). Investigation of the PSE approach for subsonic and supersonic hot jets. Detailed comparisons with LES and Linearized Euler Equations results. International Journal of Aeroacoustics, 5(4):361–393.

[Poinsot et al., 1992] Poinsot, T., Yip, B., Veynante, D., Trouvé, A., Samaniego, J. M., and Candel, S. (1992). Active control: an investigation method for combustion instabilities. J. Phys. III, 2(7):1331–1357.

[Pope, 2000] Pope, S. B. (2000). Turbulent Flows. Cambridge University Press.

[Pujals et al., 2009] Pujals, G., García-Villalba, M., Cossu, C., and Depardon, S. (2009). A note on optimal transient growth in turbulent channel flows. Physics of Fluids (1994-present), 21(1):–.

[Qadri and Schmid, 2017] Qadri, U. A. and Schmid, P. J. (2017). Frequency selection mechanisms in the flow of a laminar boundary layer over a shallow cavity. Phys. Rev. Fluids, 2:013902.

[Reynolds and Hussain, 1972] Reynolds, W. C. and Hussain, A. K. M. F. (1972). The mechanics of an organized wave in turbulent shear flow. Part 3. Theoretical models and comparisons with experiments. Journal of Fluid Mechanics, 54(2):263–288.

[Rockwell, 1983] Rockwell, D. (1983). Oscillations of impinging shear layers. AIAA Journal, 21(5):645–664.

[Rockwell and Naudascher, 1978] Rockwell, D. and Naudascher, E. (1978). Review–Self-sustaining oscillations of flow past cavities. Journal of Fluids Engineering, 100(2):152–165.

[Rockwell and Naudascher, 1979] Rockwell, D. and Naudascher, E. (1979). Self-sustained oscillations of impinging free shear layers. Annu. Rev. Fluid Mech., 11(1):67–94.

[Rossiter, 1964] Rossiter, J. (1964). Wind tunnel experiments on the flow over rectangular cavities at subsonic and transonic speeds. Technical report, Aeronautical research council reports and memoranda.

[Rowley and Williams, 2006] Rowley, C. and Williams, D. (2006). Dynamics and control of high-Reynolds-number flow over open cavities. Annual Review of Fluid Mechanics, 38:251–276.

[Sipp and Lebedev, 2007] Sipp, D. and Lebedev, A. (2007). Global stability of base and mean flows: a general approach and its applications to cylinder and open cavity flows. Journal of Fluid Mechanics, 593:333–358.

[Tam and Block, 1978] Tam, C. and Block, P. (1978). On the tones and pressure oscillations induced by flow over rectangular cavities. Journal of Fluid Mechanics, 89(2):373–399.

[Tammisola and Juniper, 2016] Tammisola, O. and Juniper, M. P. (2016). Coherent structures in a swirl injector at Re = 4800 by nonlinear simulations and linear global modes. Journal of Fluid Mechanics, 792:620–657.

[Tonon et al., 2011] Tonon, D., Hirschberg, A., Golliard, J., and Ziada, S. (2011). Aeroacoustics of pipe systems with closed branches. International Journal of Aeroacoustics, 10(2-3):201–275.

[Turton et al., 2015] Turton, S. E., Tuckerman, L. S., and Barkley, D. (2015). Prediction of frequencies in thermosolutal convection from mean flows. Phys. Rev. E, 91:043009.

[Viola et al., 2014] Viola, F., Iungo, G. V., Camarri, S., Porté-Agel, F., and Gallaire, F. (2014). Prediction of the hub vortex instability in a wind turbine wake: stability analysis with eddy-viscosity models calibrated on wind tunnel data. Journal of Fluid Mechanics, 750.